

Appraisal of breast cancer drugs and their  
precursors by Signal Amplification By  
Reversible Exchange

F Zukowicz

2021

Appraisal of breast cancer drugs and their  
precursors by Signal Amplification By  
Reversible Exchange

Filip Zukowicz

A thesis submitted in fulfilment of the requirements of  
the Manchester Metropolitan University for the degree  
of Master of Science (by Research)

Department of Natural Sciences

Faculty of Science and Engineering

Manchester Metropolitan University

2021

## **Acknowledgements**

Firstly, I would like to thank my supervisors Dr. Oliver Sutcliffe and Dr. Ryan Mewis, for providing me with the opportunity to further pursue my career goals in the field of chemistry, and for their patience and invaluable advice which helped me develop the necessary skills to finish my degree.

I would like to thank the PhD students on level 7 of the John Dalton tower, in particular Nick Gilbert and David Dixon, who have on many occasions offered me a helping hand and advice along the way.

Finally, I would like to thank my family and my partner, for the constant support and for always being there when I needed them.

## Abstract

The purpose of this study was to develop the application method of Signal Amplification By Reversible Exchange (SABRE) hyperpolarization to a pharmaceutically approved drug Letrozole. Letrozole is a drug used to treat breast cancer. It belongs to the family of drugs called aromatase inhibitors. Aromatase is the cytochrome P450 enzyme complex, which convert androgenic steroids into estrogenic steroids. Around 70% of breast cancer cells are sensitive to estrogen (or estrone - a potent endogenous estrogen), which contributes to the initiation, promotion and progression of breast cancer. Firstly, this study focused on full characterisation of 4-[(4-cyanophenyl)-(1,2,4-triazol-1-yl)methyl]benzotrile (letrozole) and on synthesis and full characterisation of the derivatives that lead up to its structure. Secondly, it was essential to develop a quantitative method of detection of all the compounds using bench top  $^1\text{H}$  Nuclear Magnetic Resonance (NMR) spectrometry. Thirdly, the largest part of the project was investigating the feasibility to hyperpolarize the compounds, focused mainly on letrozole, due to the presence of triazole functional group present in all of them. Hyperpolarization is known to lower detection limits, offer quicker and better analysis results, and cut costs when compared to regular NMR analysis. Due to the ease of use and the low costs, SABRE was the method used to achieve hyperpolarization of the compounds. The hyperpolarization of compounds 1,2,4-triazole, 1-methyl-1H-1,2,4-triazole, 1-benzyl-1,2,4-triazole, 4-(1H-1,2,4-triazol-1-ylmethyl)benzotrile, and letrozole were successful, with 1,2,4-triazole having the highest peak enhancement of -54 following polarization transfer in a 65 G field, with letrozole, which is significantly more complex in terms of its molecular architecture, having the lowest peak enhancement of -7. Only the biggest peak enhancements have been recorded for each molecule. The fact that SABRE hyperpolarization produced negative signal improvement in the  $^1\text{H}$  NMR spectrum of letrozole suggests, that the clinically

approved drug could be hyperpolarized, and potentially used in molecular imaging as a breast cancer imaging agent.

**Abbreviation and acronyms:**

AI(s) – Aromatase inhibitor(s)

cm<sup>-1</sup> – Wavenumber

ERBB2 – Erb-B2 Receptor Tyrosine Kinase 2

ER – Estrogen Receptor

ER+ – Estrogen Receptor-Positive

f<sub>0</sub> - Larmor frequency

GC-MS – Gas Chromatography-Mass Spectrometry

Hz – Hertz

HR – Hormone Receptor

IR – Infrared

M<sub>z</sub> – Longitudinal magnetisation

MP – Melting point

mL – Millilitres

mmol or mM – Millimole

NMR – Nuclear Magnetic Resonance

ppm – parts per million

RRT – Relative retention time

S, M, W, B – Infrared signal strengths; Strong, Medium, Weak, Broad

TR – Repetition Time

## Table of Contents

1. Introduction .....	9
1.1 Breast Cancer .....	9
1.1.1 Estrogen .....	12
1.2 Aromatase inhibitors .....	13
1.3 <sup>1</sup> H Nuclear Magnetic Resonance (NMR) Spectroscopy.....	16
1.3.1 Magnetic Field Alignment .....	17
1.3.2 Chemical Shifts .....	18
1.4 Hyperpolarization .....	19
1.4.1 Dynamic Nuclear Polarization (DNP) .....	19
1.4.2 Brute Force Polarization (BFP) .....	20
1.4.3 Spin Exchange Optical Pumping (SEOP).....	21
1.4.4 Chemically Induced Dynamic Nuclear Polarization (CIDNP) .....	22
1.4.5 <i>Para</i> -hydrogen Induced Polarization (PHIP) .....	23
1.4.5.1 <i>Para</i> -hydrogen And Synthesis Allow Dramatically Enhanced Nuclear Alignment (PASADENA).....	24
1.4.5.2 Adiabatic Longitudinal Transport After Dissociation Engenders Net Alignment (ALTADENA) .....	25
1.4.5.3 Signal Amplification By Reversible Exchange (SABRE).....	26

1.5 Hyperpolarization of Letrozole .....	28
1.6 Gas chromatography mass spectroscopy (GC-MS) .....	31
2. Aims and Objectives.....	33
3. Experimental .....	34
3.1 Instrumentation .....	34
3.2 Chemicals .....	35
3.3 SABRE hyperpolarization - Enhancement calculations .....	40
3.3.1 SABRE sample preparation .....	40
4. Results and Discussion .....	42
4.1 Retention times ( $R_t$ ) .....	44
4.2 Mass spectra .....	45
4.3 Infrared Spectroscopy (IR) .....	46
4.4 High Field $^1\text{H}$ NMR .....	48
4.5 Low-field $^1\text{H}$ NMR .....	53
4.6 $^{13}\text{C}$ NMR .....	55
4.7 Relaxation times $T_1$ of <b>10a - e</b> and <b>3</b> .....	56
4.8 Hyperpolarization .....	60
5. Conclusion .....	66
6. Future Work .....	67

## 1. Introduction

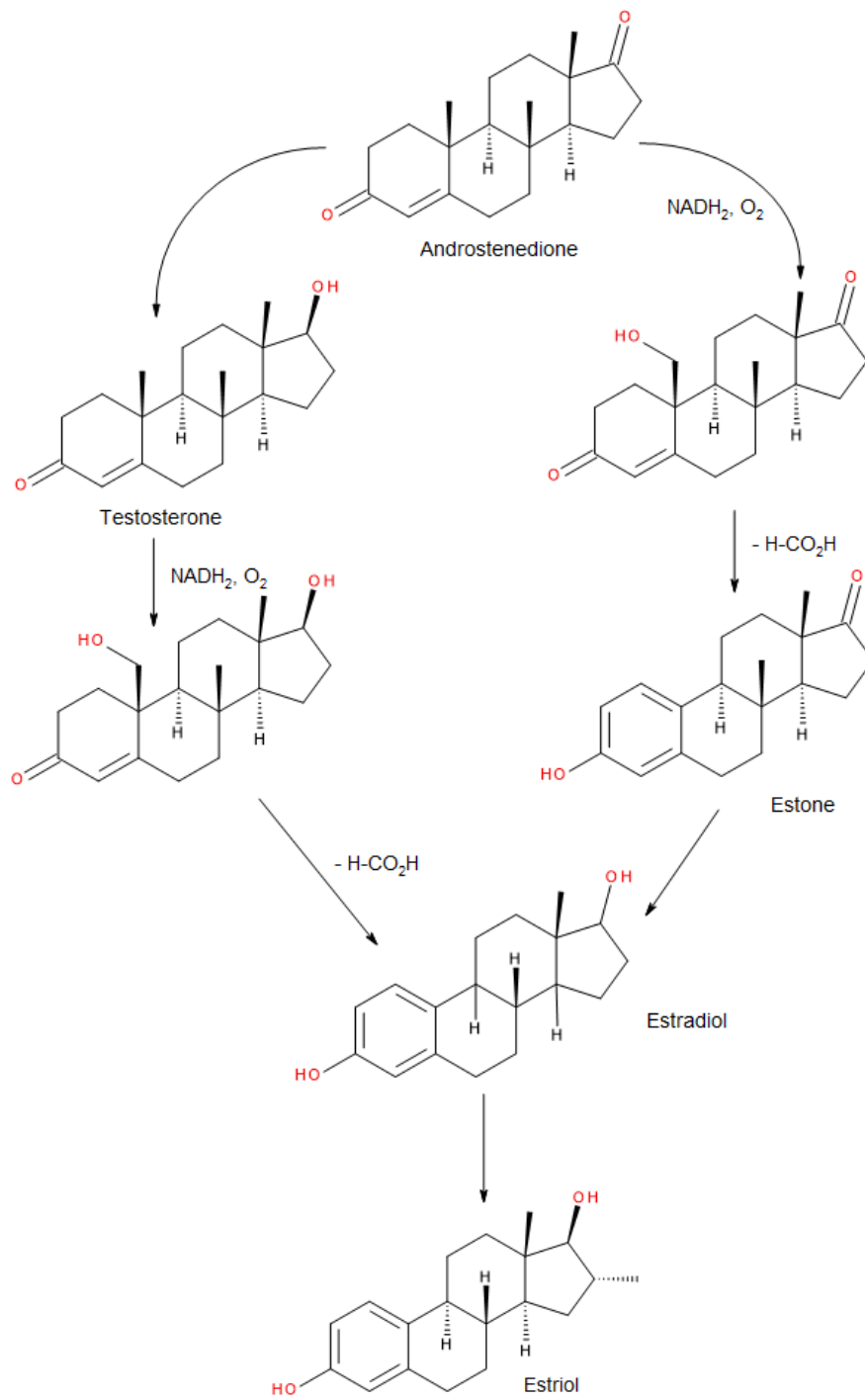
### 1.1 Breast cancer

Cancer is one of the leading causes of death worldwide with a fatality rate of 165,000 deaths every year in the UK.<sup>1,2</sup> In women, according to new cases, the most common cancer is breast cancer.<sup>3</sup> 70-80% of cases in patients with the early-stage non-metastatic disease lead to a good prognosis and a high survival rate. Advanced breast cancer with distant organ metastases is considered incurable with currently available therapies.<sup>4</sup> Breast cancer is a multifactorial disease and its occurrence is dependent on various factors, such as aging, sex, estrogen, gene mutations, family history and unhealthy lifestyle.<sup>5,6</sup> The ductal hyperproliferation is usually the prime cause of breast tumours, which when undetected, may develop into benign tumours or even metastatic carcinomas.<sup>7</sup> Recent numbers show, that the amount breast cancer cases is 100 times higher in women than that in men.<sup>8</sup>

Depending on the absence or presence, of molecular markers for progesterone or estrogen receptors (HR) and human epidermal growth factor 2 (ERBB2/HER2), breast cancer is categorised into four major subtypes: HR positive/ERBB2 negative (70% of patients), HR and ERBB2 positive (15 % of patients), triple-negative (HR and ERBB2 negative, tumours lacking all 3 standard molecular markers; 10% of patients), and HR negative/ERBB2 positive (ERBB2-enriched, 5% of patients).<sup>9,10</sup> Cells that are sensitive to estrogen contribute to the initiation, promotion and progression of breast cancer.<sup>11</sup>

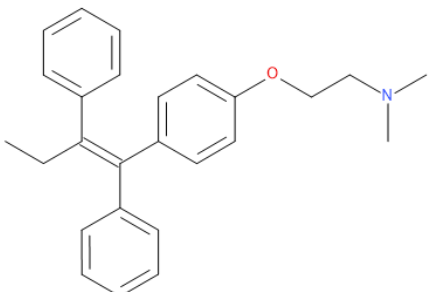
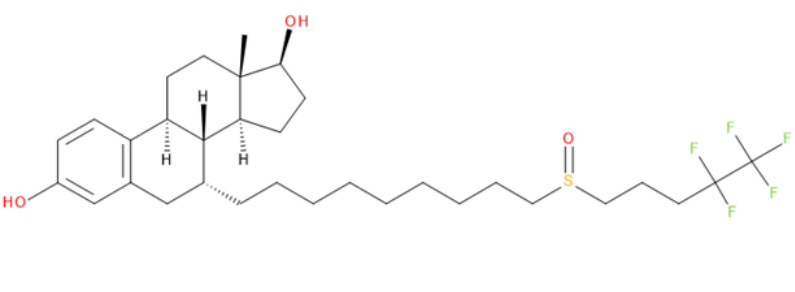
Aromatase (such as the cytochrome P450 enzyme complex – CYP19) converts C<sub>19</sub> androgenic steroids into C<sub>18</sub> estrogenic steroids (either directly or by forming testosterone first) as shown in **Figure 1**. Unlike other cytochrome P450 enzymes, this CYP19 hemeprotein has unique androgenic specificity.<sup>12</sup> The process depicted in **Figure 1** is a three-step process, which

involves the removal of the C<sub>19</sub>-methyl group (*via* two steps of hydroxylation which releases formic acid as a by-product) and aromatization of the steroid A-ring by oxidation of the 2 $\beta$ -hydrogen.<sup>13,14</sup> It has been found that the expression of aromatase is highest in or near breast tumour sites.<sup>15</sup> Over the years, different treatment methods have been invented to help the people who are suffering from breast cancer.<sup>16</sup> In the past, there were two ways in which estrogen-dependent breast cancers may have been interrupted. The first method was using selective estrogen receptor modulators (SERMs) like tamoxifen **1** (**Table 1**), to interfere with the binding of estrogen to the tumour's estrogen receptor (ER). Although recent literature describes cases of hormone resistance in breast cancer, a new generation drugs are yet to replace tamoxifen in clinical practice.<sup>17</sup> The second method was to eliminate or reduce ER expression, using fulvestrant **2**, a selective estrogen receptor down-regulator (SERD), which makes less receptors available for binding, by causing severe receptor conformational changes, promoting receptor degradation and downregulation of ER protein level.<sup>18,19</sup> In the 1970s a third method was invented, which targeted aromatase and reduced the amount of estrogen produced by the use of clinically approved selective aromatase inhibitors.<sup>20</sup>



**Figure 1.** Biosynthesis of estradiol.<sup>21</sup>

**Table 1.** Clinically approved breast cancer drugs and their corresponding structures

Name	Structure	More information
Tamoxifen <b>1</b>	 The chemical structure of Tamoxifen consists of a central carbon-carbon double bond. One carbon of the double bond is bonded to an ethyl group and a phenyl ring. The other carbon is bonded to another phenyl ring and a para-substituted phenoxy group. The phenoxy group is further substituted with a dimethylaminoethyl chain (-O-CH2-CH2-N(CH3)2).	Synthesis <sup>22</sup> Biological activity <sup>23</sup>
Fulvestrant <b>2</b>	 The chemical structure of Fulvestrant features a steroid nucleus with a hydroxyl group at the 3-position and a hydroxyl group at the 17-position. A long alkyl chain is attached at the 17-position, which is terminated by a sulfonamide group (-SO2NH2) and a pentafluorophenyl group (-C6H4F5).	Synthesis <sup>24</sup> Biological Activity <sup>25</sup>

### 1.1.1 Estrogen

Estrogens are a group of steroidal compounds that serve as the primary female sex hormones. They play an important role in the reproductive, as well as non-reproductive, systems.<sup>26</sup> Estrogens are also associated with the growth and survival of normal and cancerous breast epithelial cells by binding to the ER and activating it. In premenopausal women, estrogens are primarily produced inside the ovaries and placenta, although a small but significant amount of the compounds can also be produced by non-gonadal organs.<sup>27</sup> Naturally occurring (or endogenous) estrogens which predominate physiologically in females are: estrone (E1), estradiol (E2, or 17 $\beta$ -estradiol), and estriol (E3), shown in **Figure 1**. Each compound is biosynthesized from cholesterol *via* androstenedione and a cascade of reactions, as mentioned

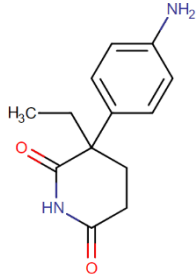
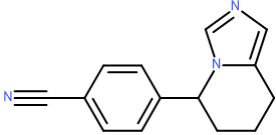
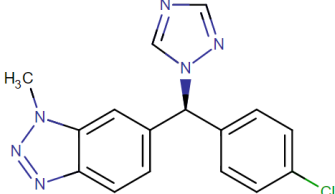
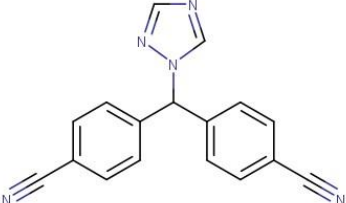
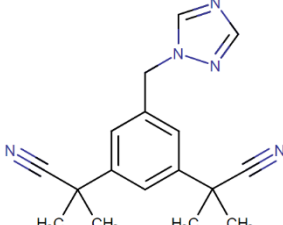
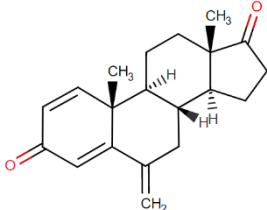
before. E2 is the major product, and the most potent estrogen produced during the premenopausal period and E1 having a bigger role postmenopause.<sup>27</sup> Estradiol functions as a circulating hormone, which acts on target distal estrogen-responsive tissues. For postmenopausal women once the ovaries stop producing estrogen and in men, this is no longer the case, and the hormone is no longer just an endocrine factor.<sup>28</sup> Instead, it acts locally (as a paracrine - cell-to-cell communication or intracrine - inside a cell communication) at extragonadal sites (such as the breasts) where it is produced.<sup>29</sup> During the biosynthesis of estrogen, the enzyme responsible for the last step in synthesis is aromatase CYP19.

### 1.2 Aromatase inhibitors (AIs)

Aromatase inhibitors (AIs) interfere with the body's ability to convert androstenedione into estrogen by suppressing aromatase enzyme activity. All non-steroidal aromatase inhibitors possess 3 N heteroatoms, located on 1,2,4-triazole as a common chemical feature.<sup>30</sup> These AIs bind to the heme iron of the cytochrome P450s with the heteroatom, interfering with steroid hydroxylations. The aromatase gene promoter in breast tissue (unlike the ovarian aromatase) is sensitive to increments in inflammatory cytokines, which increases with age, and with proliferative breast disease and breast cancer. This causes an increase in the activity of breast aromatase.<sup>30</sup>

There have been three generations of AIs developed over the years (**Table 2**) with each successive generation showing greater suppression of aromatase enzyme activity while also showing fewer side effects, making third generation AIs superior to their earlier counterparts. Non-steroidal AIs such as letrozole **3** and anastrozole **4** reversibly bind to the aromatase enzyme, and steroidal AIs like exemestane **5** do the opposite.<sup>31</sup>

**Table 2.** Different aromatase inhibitor drug generations, with their recommended dose and % of successful aromatase inhibition *in vivo* achieved at the recommended dose.<sup>30</sup>

Drug	Structure	Dose	% Inhibition
<b>First generation</b>			
Aminoglutethimide 6		1 g	91
<b>Second generation</b>			
Fadrozole 7		2 mg	82
Vorozole 8		1 mg	93
<b>Third generation</b>			
Letrozole 3		2.5 mg	99
Anastrozole 4		1 mg	97
Exemestane 5		25 mg	98

Compound **6** is considered the first-generation inhibitor or the prototype. It was originally used as an antiepileptic agent that was later removed due to side effects. One of those side-effects was the inhibition of cytochrome P450 (specifically CYP19), which begun the concept of using AIs to treat breast cancer. After the discovery of **6**, second generation inhibitors have been made (**7 & 8**), with the inhibitory activity being 700 times more potent than the previous generation. However, these compounds showed some non-selective inhibitory activity, like the reduction of plasma aldosterone, production asymptomatic orthostatic hypotension, and increase of plasma levels of androstenedione and testosterone<sup>32,33</sup>, hence the third generation of inhibitors were produced. Inhibitors **3** and **4** have a high % inhibition, with very little dose, which makes them primary treatment medicines for locally advanced ER+ breast cancer. Upon closer inspection, it was found that **3** suppressed pre-treatment tumour levels of estrone sulphate (E1S), E1 and E2 by 90.1, 90.7, and 97.6 % respectively. For comparison, **4** produced suppression levels of 72.9, 83.4, and 89.0 %, respectively.<sup>34</sup> In 2008, Dixon *et al.*<sup>35</sup> confirmed that at clinical doses, **3** is more successful at reducing plasma estrogen levels, than **4**. In a randomised, double-blind study, **3** was the only AI that was shown to have significantly superior efficacy compared to a popular selective estrogen receptor modulator (SERM) – **1** – in the neoadjuvant setting with a better response rate (60 % versus 41 %). **3** was superior to **1** in overall objective response rate (55 % versus 36 %) as well as breast-conserving surgery (48 % versus 36 %).<sup>36,37</sup> In contrast to these findings, trials did not find any significant benefit in the tumour objective response of **3** when compared to **1**. Objective response rate for **3** and **1** was 39.5% and 35.4% respectively and breast-conserving surgery became feasible in 38.1% versus 29.9% of **3**- and **1**-treated patients, respectively.<sup>34</sup> In a patient-preference study, those receiving **3** reported fewer adverse effects than those receiving **4** (43 % versus 65 % respectively), and more patients preferred **3** to **4** (68 % versus 32 % respectively).<sup>38</sup>

### 1.3 <sup>1</sup>H Nuclear Magnetic Resonance (NMR) Spectroscopy

Nuclear Magnetic Resonance (NMR) is a physical event, where a given nucleus absorbs and re-emits electromagnetic radiation. Nuclear magnetic resonance was first measured and described in 1938 by Rabi *et al.*,<sup>39</sup> who described how an oscillating magnetic field could induce a nucleus to flip their principal magnetic orientation. Yet, it was not until 1945 when NMR was successfully demonstrated. Independently, Felix Bloch and Edward Purcell detected the first significant observation of NMR in solids and paraffin, for which they were awarded the Nobel Prize in Physics in 1952, and thus begun the development of a new branch of science.<sup>40</sup> Today NMR is one of the most utilised analytical methods available, thanks to its versatility and ease of use, and it is most commonly used in structural determination and ascertaining the purity of a sample. NMR applies the quantum mechanics of subatomic particles (electrons, neutrons, and protons) due to their spin properties. In atoms such as <sup>12</sup>C, <sup>16</sup>O and <sup>32</sup>S where the spins are paired, the overall produced spin is zero as the pairs cancel each other out. Therefore, atoms which are used for routine NMR analysis are <sup>1</sup>H, <sup>13</sup>C, <sup>15</sup>N, <sup>19</sup>F, <sup>31</sup>P, etc. whose nuclei possess an overall spin of 1/2. The rule for determining the spin of a given nucleus, is if both the number of protons and neutrons are even, the nucleus will possess zero spin. If the number of protons and neutrons is odd after being added together, the nucleus will possess a half-integer spin (either 1/2, 3/2 or 5/2). If both the number of protons and neutrons are odd, the spin integer will be full (1, 2, 3).<sup>41</sup>

### 1.3.1 Magnetic Field Alignment

During the NMR analysis, a magnetic field from a radiofrequency (RF) coil is applied to the system, promoting a transition of nuclei orientated with the magnetic field (parallel to the field,  $\alpha = \alpha$ ) to those oriented against it (antiparallel to the field,  $\beta = \beta$ ) (**Figure 2**). The effect on their alignment is called the Zeeman Effect.<sup>42</sup> When the RF is turned off, the relaxation of the nuclei begins, which means the transition of nuclei from  $\beta$  orientation back to  $\alpha$ , until thermal equilibrium is reached. This process generates radiofrequencies, which are recorded by the NMR spectrometer and are displayed as a spectrum, following Fourier transformation.<sup>42</sup>

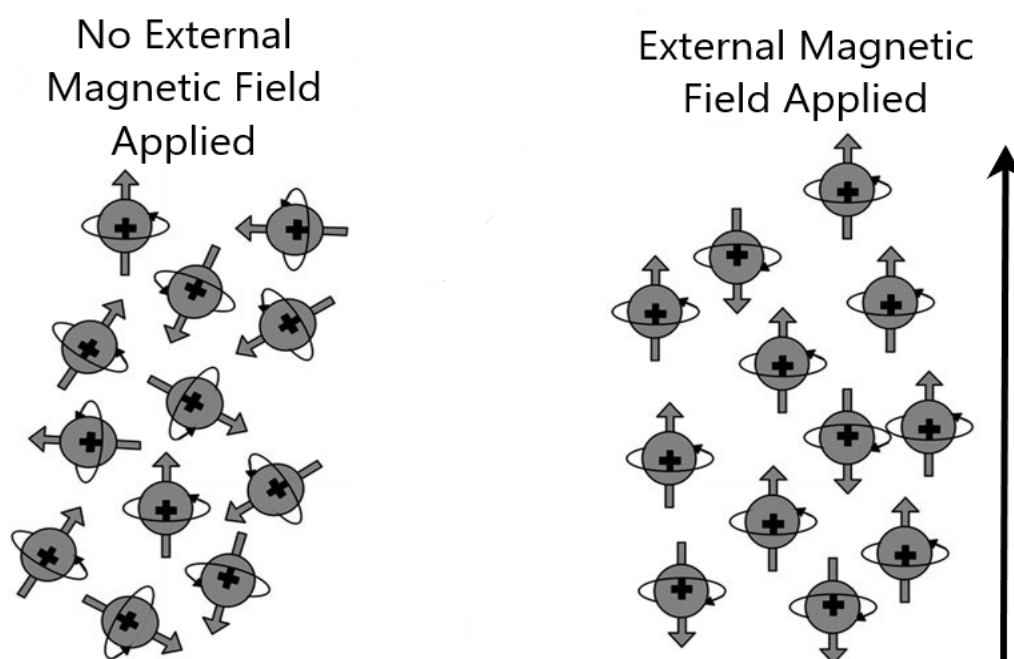


**Figure 2.** A simplified diagram showing alignment of protons due to an external magnetic field. Adapted from the publication by D. A. Pollacco (2016)<sup>43</sup>

### 1.3.2 Chemical Shifts

The radiofrequency which is detected in NMR spectroscopy is proportional to the magnetic field applied to the nucleus. Thus, it could be assumed that the resonance signal of a specific nucleus would have the same frequency value every time, feeding back to the user unhelpful information. However, due to chemical shift, multiplicity, the number of signals present and integral values, scientists can identify and characterise structures from their NMR signature. When applying an external magnetic field, the electrons respond in a way such that their motions produce a small magnetic field at the nucleus that usually acts in opposition to the externally applied field.<sup>40</sup> Due to the change in the effective field on the nuclear spin, the signal frequency reported in the NMR spectrum shifts. The magnitude of the shift depends on the type of nucleus responding to the external magnetic field and the electron motion in the surrounding environment of atoms. The magnetic field produced by the electrons acts to either shield or deshield the nucleus. It is understood that with more shielding, a greater frequency is needed to bring the nuclei on resonance (i.e. lower chemical shift). Aliphatic nuclei, such as the methyl proton nuclei of an ethyl chain, are shielded in this way as the magnetic field produced by the electrons opposes that of the external magnetic field. Conversely, less shielded nuclei, such as aromatic nuclei, are deshielded (i.e. higher chemical shift) as the magnetic field produced by the electrons act to reinforce the external magnetic field.<sup>44</sup> Thus, a lower frequency is required to bring these nuclei on resonance.

## 1.4 Hyperpolarization

One of the limitations of NMR is its low sensitivity when compared to optical spectroscopic methods, which is caused by the very small population differences that exist between nuclear spin states. A way to improve the sensitivity of the NMR is through hyperpolarization. Hyperpolarization is the nuclear spin polarization of a material in a magnetic field, which exceeds the thermal equilibrium conditions determined by the Boltzmann distribution.<sup>45</sup> Hyperpolarization of solids, liquids, and gases can be achieved *via* a number of techniques: Dynamic Nuclear Polarization (DNP), Brute Force Polarization (BFP), Spin Exchange Optical Pumping (SEOP), Chemically Induced Dynamic Nuclear Polarization (CIDNP), *Para*-hydrogen Induced Polarization (PHIP) and Signal Amplification By Reversible Exchange (SABRE).<sup>45</sup>

### 1.4.1 Dynamic Nuclear Polarization (DNP)

In Dynamic Nuclear Polarization (DNP), polarization is transferred from a radical species to the substrate of interest *via* terahertz microwave irradiation near or at the Electron Paramagnetic Resonance (EPR) transition (more specifically a single quantum EPR transition which exists between a hyperfine coupled electron and nuclear spin).<sup>46</sup> This process can take upwards of hours to complete to a satisfactory polarization level. The sample of interest is polarized by dissolving or suspending it in glass-forming matrices doped with polarizing agents (typically a stabilised radical) at low temperature (100 K or less).<sup>46</sup> DNP was developed with a focus on frozen liquid samples and solid-state samples. DNP enhancements can reach several orders of magnitude under the right conditions (by up to 50,000-fold compared to thermal polarization)<sup>47</sup>, but there are some limiting factors which have to be overcome before it could be widely applied to drug discovery studies.<sup>46</sup> Nuclei with short spin-lattice relaxation

time ( $T_1$ ) are difficult or near-impossible to detect, therefore identification of unknown compounds could prove to be challenging. The pre-condition of radical insertion to the sample is also an undesirable action after time-consuming purification of a product. This makes DNP an unfavourable method for NMR analysis, but is applicable to MRI, as it increases the sensitivity of  $^{13}\text{C}$ , which has a naturally low-background signal in the body.<sup>48</sup>

#### 1.4.2 Brute Force Polarization (BFP)

Brute Force Polarization (BFP) is the simplest hyperpolarization method as it involves modification of magnetic field ( $B$ ) and temperature ( $T$ ) to generate hyperpolarization. With reference to **Equation 1**,  $B$  and  $T$  are the only terms that can be manipulated, as  $\gamma$  is the gyromagnetic ratio of the nucleus being examined,  $h$  is Planck's constant and  $k_B$  is the Boltzmann constant.

$$\text{Equation 1. } P = \left( \frac{\gamma h B_0}{2k_B T} \right)$$

BFP takes place in a high magnetic field ( $B > 14$  Tesla (T)) and at a low temperature ( $T \leq 4$  K).<sup>49</sup> Lowering  $T$  prevents the population of higher energy level (linked to  $\beta$ -orientated spins) due to thermally linked effects, and increasing  $B$  helps with the promotion of  $\alpha$ -orientated spins to  $\beta$ -orientated spins. Unlike DNP, no microwave excitation, free-radicals, or co-solvents are needed. This creates three obvious advantages. Firstly, there is no requirement to chemically alter the sample analyte. Secondly, due to BFP relying only on Boltzmann-law it is not limited to any specific types of samples. Thirdly, the absence of radicals avoids the need for downstream filtering and quality assurance.<sup>49</sup> As **Table 3** shows, BFP can deliver substantial gains in polarization. However, BFP does have limitations. Obtaining the required low

temperatures is challenging for hardware and requires cryogenic cooling. Some solvents are unsuitable e.g. dimethylsulfoxide due to incompatible freezing points. Furthermore, utilising strong magnetic fields for performing the NMR analysis requires substantial financial outlay.

**Table 3.** Polarization of  $^1\text{H}$  and  $^{13}\text{C}$  at different magnetic fields.

Nucleus	Polarization at $B_0=1.5\text{ T}$ ; $T=310\text{ K}$	Polarization at $B_0=20\text{ T}$ ; $T=4\text{ K}$
$^1\text{H}$	$4.9 \times 10^{-6}$	$5.1 \times 10^{-3}$
$^{13}\text{C}$	$1.2 \times 10^{-6}$	$1.3 \times 10^{-3}$

#### 1.4.3 Spin Exchange Optical Pumping (SEOP)

Spin Exchange Optical Pumping (SEOP) is the most commonly used method for generating hyperpolarized noble gases. SEOP development began when Kastler, who was awarded with the Nobel Prize for his work, demonstrated, that using circularly polarized laser light, an electronic spin order can be created in alkali metal vapours.<sup>50</sup> Later discoveries showed, that adding  $^3\text{He}$  to the optically pumped alkali vapour atoms permitted polarization of  $^3\text{He}$  nuclear spins by spin-exchange collisions. This work has been extended to  $^{129}\text{Xe}$ , leading to the ability to produce large numbers of hyperpolarized noble gases with nuclear spin polarization levels. SEOP has advanced the resolution of MRI as noble gases, such as  $^3\text{He}$  and  $^{129}\text{Xe}$ , offer an improved method of determining the health and condition of lungs.<sup>51</sup> This is important in a number of disease states, such as emphysema and cystic fibrosis. When compared to conventional MRI, which does not give any anatomical information of the inner lung space

due to the low concentration of nuclei that can be interrogated (e.g.  $^1\text{H}$ ) and computed tomography, which only images the first six branches of the lung, SEOP can image all 23 branches of the lung using hyperpolarized noble gases. These gases, such as  $^3\text{He}$  and  $^{129}\text{Xe}$ , are used as imaging agents and offer clear and high-resolution images. Due to these gasses SEOP is a favoured method over DNP, when producing MRI agents.<sup>52</sup>

#### **1.4.4 Chemically Induced Dynamic Nuclear Polarization (CIDNP)**

Chemically Induced Dynamic Nuclear Polarization (CIDNP) is defined as a non-Boltzmann nuclear spin state distribution produced under thermal conditions or through a photochemical reaction. Due to the highly nonperturbative nature, and short hyperpolarization time of  $\sim 10^{-6}$  s, CIDNP has recently received considerable attention as a hyperpolarization tool for aromatic polypeptides, proteins, and amino acids in solution. It also provides a very useful tool for investigating radical pairs and elusive radicals.<sup>53</sup> CIDNP works by forming a radical pair (RP) with a photoexcited photosensitizer.<sup>54</sup> The nuclei experiencing notable hyperfine interactions with the unpaired electron will be the only one to experience the hyperpolarization, where the signal enhancements are usually proportional to the coupling constant. The photodegradation and the lack of uniform irradiation of the whole sample are the two main limitations of CIDNP. These limitations require alternative approaches to be considered for different analytes.<sup>54</sup>

### 1.4.5 *Para*-hydrogen Induced Polarization (PHIP)

*Para*-hydrogen Induced Polarization (PHIP) is a technique of hyperpolarization that depends on fast chemical reactions, that enables pairwise addition of *para*-hydrogen across unsaturated chemical bonds adjacent to  $^{13}\text{C}$  carboxyl or  $^{15}\text{N}$  nuclei (**Figure 3**). *Para*-hydrogen protons are paired in a singlet spin-state, which has no magnetic moment, which means they do not give rise to a signal when analysed *via* NMR.<sup>55</sup> PHIP is more suited for chemical analysis and characterisation due to its speed, which is one of its main advantages, while the main disadvantage is the requirement for an unsaturated molecular PHIP precursor with appropriate asymmetry (for example 1,3-butadiene<sup>56</sup>).<sup>57</sup> This proves to be a significant limitation for biological applications, although newly developed concepts using -OH protection in -C=C-O-R have significantly expanded the reach of molecular targets for PHIP.<sup>58</sup> PHIP has three different approaches: *Para*-hydrogen And Synthesis Allow Dramatically Enhanced Nuclear Alignment (PASADENA), Adiabatic Longitudinal Transport After Dissociation Engenders Net Alignment (ALTADENA) and Signal Amplification By Reversible Exchange (SABRE).<sup>57</sup> PASADENA and ALTADENA are hydrogenative forms of PHIP, whereas SABRE is non-hydrogenative. In PASADENA, polarization transfer occurs at high-magnetic field (i.e. in the magnet of the NMR spectrometer) alongside the detection of the polarized state. For ALTADENA and SABRE, polarization transfer occurs outside of the magnet (i.e. at low magnetic field) prior to rapidly transporting the sample to high-magnetic field for interrogation of the polarized state. SABRE is often considered the non-hydrogenative form of ALTADENA.

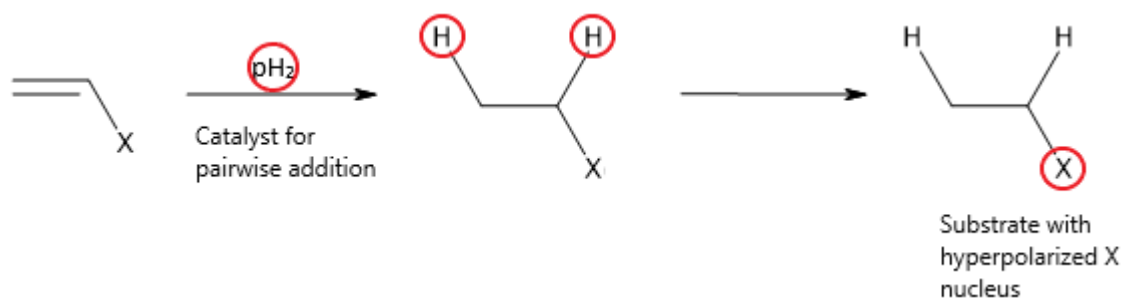


**Figure 3.** Schematic of the *para*-hydrogen-induced polarization (PHIP) process. Adapted from the publication by Kovtunov *et. al.* (2019)<sup>56</sup>

#### 1.4.5.1 *Para*-hydrogen And Synthesis Allow Dramatically Enhanced Nuclear Alignment (PASADENA)

*Para*-hydrogen And Synthesis Allow Dramatically Enhanced Nuclear Alignment (PASADENA) is a unique method among other hyperpolarization methods due to its combination of effectiveness, speed, spectral quality, and the simplicity of the apparatus. PASADENA reaches high nuclear polarization within seconds in the liquid state by transforming the spin order of *para*-hydrogen to net polarization of a third nucleus like <sup>13</sup>C by means of a spin-order-transfer (SOT) sequence.<sup>59</sup> PASADENA is mostly used to study homogeneously catalysed hydrogen reactions and is characterised by the use of low-field and high-field magnets. This method is used for signal enhancement (up to a factor of 100,000-fold on currently utilized MRI scanners)<sup>59</sup> but can also be used to evaluate reaction mechanisms and the kinetics involved in the reaction. The amplitude of the signal depends critically on the ratio of the J-coupling, which is an indirect interaction between two nuclear spins, that arises from interactions between the nuclei and bonding electrons.<sup>59</sup> The limitation to this method is that it is

intrusive. The substrate is chemically changed after the addition of *para*-hydrogen, therefore reducing its effectiveness in certain areas of research.<sup>60</sup>

#### **1.4.5.2 Adiabatic Longitudinal Transport After Dissociation Engenders Net Alignment (ALTADENA)**

Adiabatic Longitudinal Transport After Dissociation Engenders Net Alignment (ALTADENA) is a method similar to PASADENA, which also requires an unsaturated substrate, as hydrogenation with *para*-hydrogen of an unsaturated bond is fundamental. The difference between them is the hyperpolarization method, seen in **Figure 4**. ALTADENA uses a non-equilibrium population difference when hydrogenation at low magnetic field is followed by adiabatic transfer of the hydrogenated product to high magnetic field. This method adopts a concept known as 'isotropic mixing'. In practice, samples can be polarized in the stray field of an NMR magnet, followed by the detection of the hyperpolarized state in a high-field magnet after the application of appropriate pulse sequences.<sup>61</sup> Although ALTADENA is very similar to PASADENA regarding hyperpolarization, when comparing spectra obtained through the two methods, it is clear that ALTADENA is more efficient. This is due to the sample being slowly transferred towards the NMR magnet, where polarization differences are created, and their amplitude can be larger. It is stated that high *para*-hydrogenation rates for both PASADENA and ALTADENA significantly increase the transfer of PHIP to heteronuclei.<sup>62</sup>

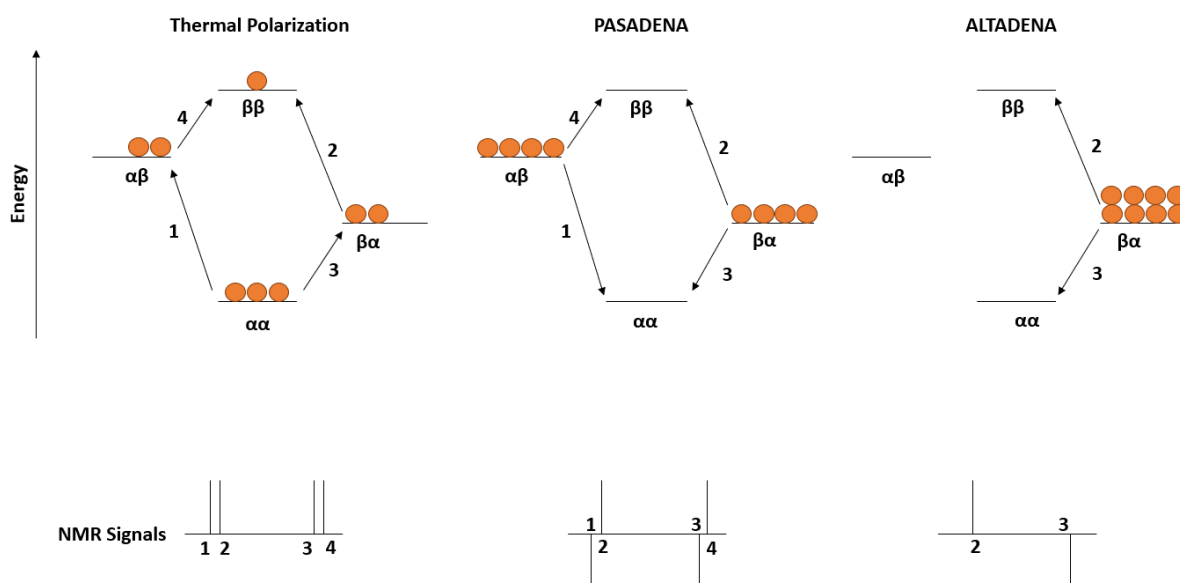


**Figure 4.** Schematic representation of the NMR characteristics and spin configurations. In ALTADENA only the lower energy  $\beta\alpha$  spin state is populated. Under ALTADENA conditions, only two components are observed for each resonance, each with a different phase. The conditions corresponding to PASADENA result in the obtained  $^1\text{H}$  NMR signals possessing characteristic out of phase signals, appearing as two equally intense pairs; one line pointing upwards for absorption, and a second pointing downwards, for emission. Adapted from the publication by Fekete *et. al.* (2015)<sup>63</sup>

#### 1.4.5.3 Signal Amplification By Reversible Exchange (SABRE)

Signal Amplification By Reversible Exchange (SABRE) is another *para*-hydrogen based hyperpolarization technique, which enhances sample detectability. SABRE differs from PASADENA and ALTADENA as it is non-hydrogenative. SABRE predominantly uses iridium-centred catalysts to propagate polarization transfer.<sup>55</sup> These catalysts enable exchange of substrate and *para*-hydrogen-derived hydrides at the metal centre. Polarization is transferred

from the *para*-hydrogen-derived hydrides to substrate spin 1/2 nuclei through the J-coupling network that is established. A weak polarization transfer field (typically  $65 \times 10^{-4}$  T for  $^1\text{H}$ ) is used to facilitate polarization transfer. Substrate molecules *trans* to *para*-hydrogen-derived hydrides are optimally polarized whereas those that are *cis* receive no polarization (as the J-coupling is effectively zero). The polarization is transferred from *para*-hydrogen derived hydride ligands to the protons of an analyte *trans* to it *via* the establishment of J-coupling (scalar) network (**Figure 5**).<sup>64</sup> Hyperpolarization is acquired by dissolving *para*-hydrogen in a solution containing the target analyte within a weak polarization transfer field (typically  $65 \times 10^{-4}$  T for  $^1\text{H}$ ) and the active SABRE catalyst.<sup>64</sup>

The iridium catalyst (**Figure 5**) has undergone extensive development to tune ligand and hydride exchange rates to maximise polarization transfer. The catalyst enables biocompatible SABRE hyperpolarization with heterogeneous catalyst in aqueous media with the ability to recycle the catalyst.<sup>65</sup> This method provides renewable hyperpolarization provided the *para*-hydrogen atmosphere is refreshed routinely. Notably, unlike PHIP, SABRE does not lead to the chemical composition of the analyte becoming changed. This entails a much larger scope of molecules that can be investigated as it does not need an unsaturated bond to be present.<sup>66</sup> The use of a catalyst does not increase the experimental time greatly, as the activation can occur at ambient temperatures (catalyst decomposes upon heating)<sup>67</sup> and without the need of advanced equipment.

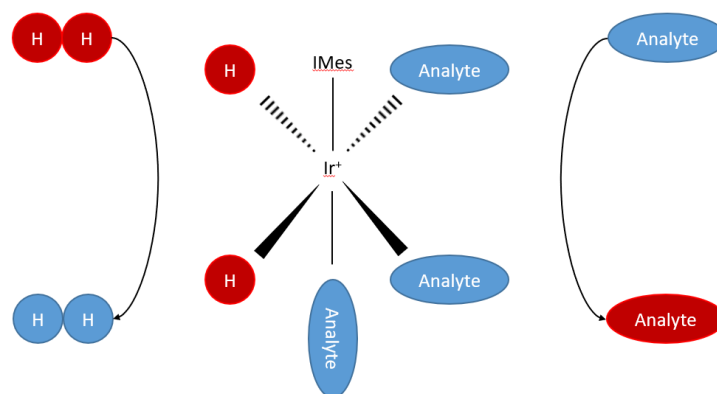


**Figure 5.** Simplified diagram of SABRE hyperpolarization with iridium catalyst (centre).

Adapted from the publication by Semenova *et. al.* (2018)<sup>66</sup>

### 1.5 Hyperpolarization of Letrozole

One of the major challenges in cancer biology is monitoring and understanding cancer metabolism *in vivo* with the sole goal of improved diagnosis and therapy. Tracer methods are required to detect specific enzyme-catalysed reactions, as the crucial metabolites (L-octanoylcarnitine, 5-oxoproline, hypoxanthine, and DHA)<sup>68</sup> are low in concentration and, therefore, beyond the detection range of traditional magnetic resonance methods. A solution to this is hyperpolarization, which can improve sensitivity by a factor of 10,000 or more.<sup>69</sup> All the methods mentioned in sections 1.4.1-1.4.5.3 can induce hyperpolarization. However, the hyperpolarized state value decreases with a time constant according to the spin-lattice relaxation time ( $T_1$ ) once the hyperpolarized compound is delivered *in vivo*. Because of this, the signal may be significantly reduced during *in vivo* detection to unmeasurable levels. This gives rise to challenges in that  $T_1$  has to be long enough so that a large enough number of hyperpolarized states is preserved *in vivo*, or that the relevant pathways or processes being studied must occur sufficiently quickly so that useful information can be obtained. Although  $T_1$  is a big imaging limitation for *in vivo* studies, unlike nuclear medicine probes, the images

can be taken without waiting for the clearance of hyperpolarized probes. The hyperpolarized probes are produced *ex situ* and introduced into biological systems, allowing images to be taken immediately after the administration of the probe. The probes are detected with high sensitivity and contrast against background signals providing information on biodistribution, uptake and metabolism of the probe in a scan time of a minute or less.<sup>70</sup> This approach provides clear advantages, such as the ability to image metabolic activity of cells immediately after the administration of the probe or the observation of a fast-metabolic flux. In many cases, it was found that the polarization of <sup>13</sup>C and <sup>15</sup>N molecular sites would persist for much longer compared to other nuclei, such as protons, with a hyperpolarization relaxation time of a few seconds or less. This is due to <sup>13</sup>C and <sup>15</sup>N possessing a low gamma ( $\gamma$ ) compared with that of <sup>1</sup>H. As polarization is a product of low- $\gamma$  of the nucleus being studied and the applied magnetic field strength in which the nuclei are situated, weak signals can be enhanced by transfer of polarization from spins with high magnetic moments (<sup>1</sup>H) to nuclear spins with lower magnetic moments (<sup>13</sup>C and <sup>15</sup>N).<sup>69,70</sup> In previous reports, it was found that <sup>15</sup>N sites interact directly with the iridium catalytic centre of the polarization transfer catalyst [Ir(IMes)(COD)Cl] (COD = *cis,cis*-1,5-cyclooctadiene, IMes = 1,3-*bis*(2,4,6-trimethylphenyl)imidazole-2-ylidene), which is used in SABRE experiments.<sup>69</sup> This catalyst facilitates the polarization transfer from *para*-hydrogen derived hydrides to <sup>15</sup>N sites. Pyridine was one of the first compounds to be polarized by SABRE, followed by other studies using numerous pyridine derivatives.<sup>71</sup> These experiments have shown that pyridyl-analogues antibiotics e.g. metronidazole (2-(2-methyl-5-nitroimidazol-1-yl)ethanol **9**), has been polarized to a level of 15%, compared to non-hyperpolarised thermal spectra, which persists for tens of minutes at 1.4 T when applied SABRE hyperpolarization when compared to its non-hyperpolarised thermal spectra.<sup>71</sup> It is important to note the concentration of <sup>15</sup>N nuclei is consistent. These

results give strong foundations for letrozole to successfully hyperpolarize due to its triazole ring, which can be mapped onto pyridine or molecule **9** seen in **Figure 6**, which is an excellent delivery vehicle because its three  $^{15}\text{N}$  sites carry thrice the hyperpolarization payload of (single-site) pyridine derivatives.<sup>72</sup>

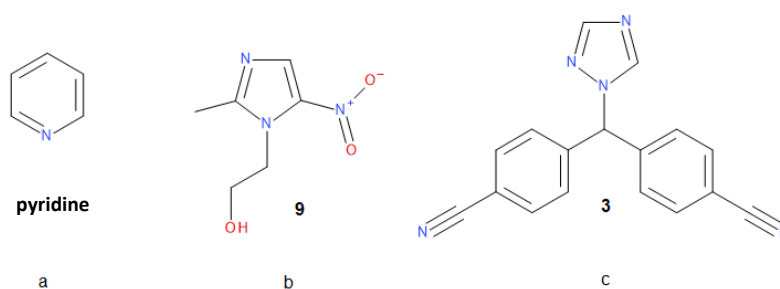


**Figure 6.** Structures of pyridine (a), **9** (b) and **3** (c). The  $^{15}\text{N}$  sites on (a) and (b) can be hyperpolarized with relaxation time constants ranging from 1 min to 10 min. Due to the similarities in the nitrogen rings, it was reasonable to assume that **3** will hyperpolarize.

Another factor which could help predict how well a molecule could be hyperpolarised is the pKa values. The pKa values of pyridine, imidazoles and triazoles are 5.2, 6.9 and 9.3 respectively.<sup>73</sup> Pyridine's low pKa value, means it is the strongest Lewis acid out of the three rings and it will accept the electrons the best. This positively affects the hyperpolarisation strength, making pyridine one of the best compounds in terms of hyperpolarisation strength.<sup>74</sup> Imidazole has a higher pKa than that of pyridine hence it doesn't accept electrons as strongly as pyridine, making the hyperpolarisation strength lesser than pyridine's. Triazole's pKa of 10.3 is the highest. When following the trend, triazole will hyperpolarize to a smaller degree, because it is less able to accept the electrons when bound to the metal catalyst.

## 1.6 Gas chromatography mass spectroscopy (GC-MS)

Gas chromatography mass spectroscopy (GC-MS) was one of the methods utilised to characterise compounds used in this thesis. GC-MS is a technique that is used when analysing several similar compounds, due to chromatogram's high precision and accuracy for GC active compounds. This analytical method was used to analyse the synthesized products in order to confirm the successful synthesis as well as the purchased compounds to ensure they could be used without the need for purification. All the compounds analysed in this report have a similar structure, making the use of GS-MS, a valid characterisation method. GC-MS is split into two components: The Gas Chromatograph (GC) and the Mass Spectrometer (MS) (**Figure 7**).

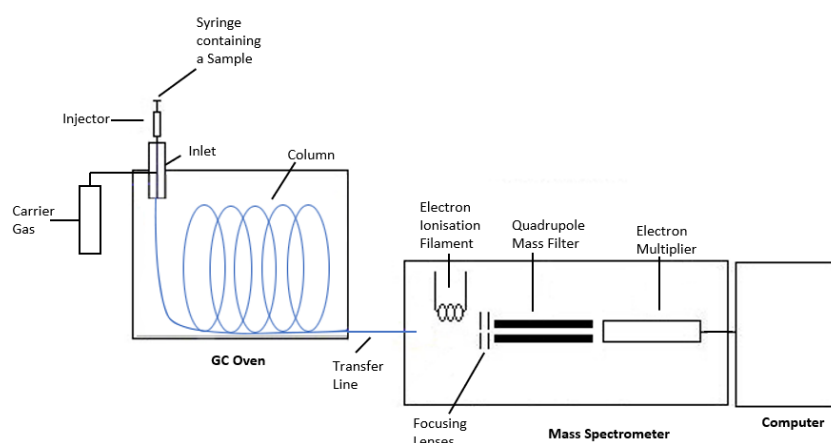


**Figure 7.** A simplified diagram of GC-MS with the key components labelled. Figure adapted from a diagram by Emwas *et al.*<sup>75</sup>

The Gas Chromatograph is responsible for separating a mixture of analytes based on their relative volatilities. The sample is injected into the GC using the syringe and is then mixed with the mobile phase (carrier gas) inside the inlet, which then carries the sample into the column. The analytical column has a stationary phase coated on the inside walls. The analytical column is held in the GC oven that is heated during the analysis to elute the less volatile components.

The details of the method can be seen in **Section 3.2**. The outlet of the column is inserted into the detector located at the transfer line that responds to the chemical components eluting from the column to produce a chromatogram. As the compounds elute and pass through the detector (in this case the MS) the concentration of molecules which are detected is directly proportional to the peak area. The result is a chromatograph, which is a plot of relative response over the retention time ( $R_t$ ).

The Mass Spectrometer component of the GC-MS system is a specialised detection method used to identify the structure of analytes as they elute from the GC-column. The molecules that elute from the GC column are first ionised within the ion source (a beam of electrons) to produce positively charged molecular ions which rapidly degrade into fragment ions – this is known as electron impact ionisation. The fragment and molecular ions are then separated in the mass analyser based on their mass/charge ( $m/z$ ) ratio.

## 2. Aims and Objectives

The aim of this thesis was to demonstrate that the clinically approved drug **3** could be hyperpolarized *via* SABRE, to obtain a hyperpolarized  $^1\text{H}$  NMR spectra, as well as to investigate if the size of molecules affect the amount of hyperpolarization when using the same hyperpolarization method.

The objectives were to hyperpolarize molecule **3** and determine the amount of hyperpolarization by measuring the peak enhancement ( $\epsilon$ ) and to collect data for the compounds 1,2,4-triazole **10a**, 1-methyl-1H-1,2,4-triazole **10b**, 1-benzyl-1,2,4-triazole **10c**, 4-(1H-1,2,4-triazol-1-ylmethyl)benzotrile **10d**, 1-[di(phenyl)methyl]-1H-1,2,4-triazole **10e** using the same method, and using the acquired data to devise a pattern in between the molecule size and  $\epsilon$ .

### 3. Experimental

#### 3.1. Instrumentation

All NMR spectra for characterisation of synthesised compounds were collected on a JEOL ECS-400 FT NMR in the solvent described with chemical shifts ( $\delta$ ) quoted in ppm and coupling constants (J) quoted in hertz (Hz). Spectra were collected at a frequency of 400.14 MHz for  $^1\text{H}$  spectra and 101 MHz for  $^{13}\text{C}$  spectra.

SABRE NMR spectra were collected on an Oxford Instruments Pulsar benchtop at a frequency of 59.8 MHz for  $^1\text{H}$  spectra. NMR analysis was carried out making use of MestReNova version 11.0.4 and ACD/Labs version 2020.1.2. SABRE measurements above earth's magnetic field were accomplished using a custom electromagnet produced by Siga Transformers ([sigatransformers.co.uk](http://sigatransformers.co.uk)) within which a vertical magnetic field of up to 150 G could be generated. A Hirst Magnetic Instruments Ltd GM07 gaussmeter serial #10620 with transverse (Hirst magnetic instruments Ltd, Cornwall, UK) and axial stock number 212-736 (RS components Ltd, Northants, UK) hall probes were used to determine the exact magnetic field for measurements which involved polarization transfer occurring under SABRE conditions.

Purification was carried out using flash chromatography performed on a Biotage Isolera One System equipped with Isolera Assist (Biotage GB Limited, Hengoed, CF82 7TS) using Biotage Sfär columns and a mobile phase consisting of EtOAc:hexane (1:3).

Hydrogen was generated using a Peak scientific PH200 hydrogen generator (Peak Scientific Instruments Ltd, Inchinnan, UK) set to 3.5 bar. Where *para*-hydrogen was required this was generated through the immersion of a charcoal packed coil into liquid nitrogen to generate

~50% enriched *para*-hydrogen. SABRE measurements were made utilising GPE scientific, 5mm, 7" long, 400 MHz, Norell select series Young's tubes.

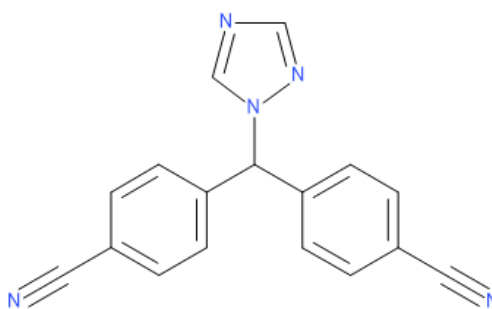
Gas Chromatography – Mass Spectrometry (GC-MS) analysis was performed on an Agilent 7890B GC coupled to an Agilent 5977B Mass Spectrometer (Agilent Technologies, Cheadle, UK). The GC-MS method was carried out using 0.5  $\mu$ L injection split 50:1 with an inlet temperature of 265 °C. A hold time of 3 minutes at 50 °C was utilised, with ramps of 30 °C/min for 8 minutes, then a further hold time of 6 minutes at 290 °C. Helium was used as a carrier gas at a rate of 1.2 mL/min through a HP5-MS column (30 m x 0.25 mm x 0.25  $\mu$ m).

Infrared analysis was performed on a PerkinElmer FTIR (PerkinElmer, Llantrisant, UK) with 4 scans acquired across the range 4000 – 400  $\text{cm}^{-1}$ .

### 3.2 Chemicals

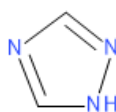
All materials were sourced from Acros Organics (Loughborough, UK), Sigma-Aldrich (Gillingham, UK), Fisher Scientific (Loughborough, UK) or Apollo chemicals (Tamworth, UK). All materials were used as received unless stated within the experimental procedure. The SABRE pre-catalyst,  $[\text{Ir}(\text{IMes})(\text{COD})\text{Cl}]$ , was prepared by Dr. Thomas Robertson<sup>76</sup> and used as received. Solvents were purchased from Fisher Scientific and were of general use or HPLC grade unless specifically stated. Where the use of dry ethyl acetate is stated, it was dried over anhydrous potassium carbonate and then distilled prior to use. TLC analysis made use of aluminium backed silica gel 60 F<sub>254</sub> plates (Merck Millipore). Deuterated solvents were sourced from Sigma Aldrich with  $\geq 99.8\%$  deuterium labelling.

#### 4-[(4-Cyanophenyl)-(1,2,4-triazol-1-yl)methyl]benzonitrile (Letrozole, 3)



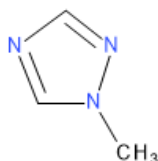
4-[(4-Cyanophenyl)-(1,2,4-triazol-1-yl)methyl]benzonitrile (Letrozole) was obtained from Fluorochem (Glossop, UK) [Batch No. H1377] and used without further purification.  $^1\text{H}$  NMR (400 MHz,  $\text{CD}_3\text{OD}$ )  $\delta$  (ppm): 8.50 (1H, s, NCHN), 7.99 (1H, s, NCHN), 7.67 (4H, d, CH), 7.34 (4H, d, CH), 7.12 (1H, s, CH);  $^{13}\text{C}\{^1\text{H}\}$  NMR (100.5 MHz,  $\text{CD}_3\text{OD}$ )  $\delta$  (ppm): 153.1, 145.9, 144.2, 133.8, 130.4, 119.1, 113.7, 66.8; ; ATR-FTIR  $\nu$  ( $\text{cm}^{-1}$ ): 3120 (CH, m), 2231 (CN, s), 1743-1607 (CH, w, aromatic overtones), 1275 (C=N, s); MS ( $m/z$  - ESI): 217 (BS), 284 ( $\text{M}^+$ ), 285 ( $[\text{M}+\text{H}]^+$ ); RRT: 1.41; mp 187 – 191 °C [183 – 185 °C (lit.<sup>77</sup>)].

#### 1,2,4-Triazole (10a)



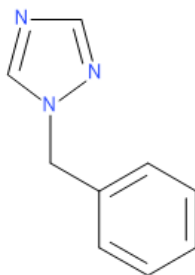
1,2,4-Triazole was obtained from Fluorochem (Glossop, UK) [Batch No. FCB033416] and used without further purification.  $^1\text{H}$  NMR (400 MHz,  $\text{CD}_3\text{OD}$ )  $\delta$  (ppm): 8.10 (2H, s, NCHN);  $^{13}\text{C}\{^1\text{H}\}$  NMR (100.5 MHz,  $\text{CD}_3\text{OD}$ )  $\delta$  (ppm): 147.6; ATR-FTIR  $\nu$  ( $\text{cm}^{-1}$ ): 3128 (CH, m), 3119-3032 (CH, m), 2966-2653 (NH, m), 1765 (CH, w), 1270 (C=N, s); mp 125 – 129 °C [120 – 121 °C (lit.<sup>78</sup>)].

### 1-Methyl-1H-1,2,4-triazole (10b)



1-Methyl-1H-1,2,4-triazole was obtained from Fluorochem (Glossop, UK) [Batch No. FCB044065] and used without further purification.  $^1\text{H}$  NMR (400 MHz,  $\text{CD}_3\text{OD}$ )  $\delta$  (ppm): 8.27 (1H, s, NCHN), 7.86 (1H, s, NCHN), 3.79 (3H, s,  $\text{CH}_3$ );  $^{13}\text{C}\{^1\text{H}\}$  NMR (100.5 MHz,  $\text{CD}_3\text{OD}$ )  $\delta$  (ppm): 152.0, 145.4, 36.4; ATR-FTIR  $\nu$  ( $\text{cm}^{-1}$ ): 3114 (CH, w), 2949 (CH, w), 1511 (CH, s), 1272 (C=N, s); mp 21-22 °C [20 °C (lit<sup>79</sup>.)].

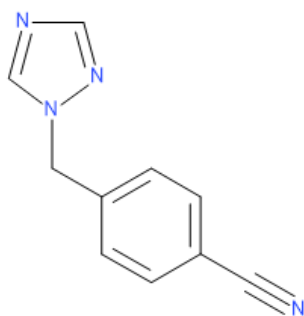
### Synthesis of 1-benzyl-1,2,4-triazole (10c)



The target compound was prepared using the method reported by Wood *et al.*<sup>80</sup> Sodium-1,2,4-triazole (1.06 g, 15.3 mmol), potassium carbonate (1.41 g, 10.2 mmol) and potassium iodide (0.10 g, 0.60 mmol) were sequentially added to benzyl bromide (1.74 g, 10.20 mmol) in acetone (50 mL). The reaction mixture was heated at 55 °C and left to stir for 24 h. The solution was left to cool, followed by addition of water (100 mL). The product was extracted using ethyl acetate (EtOAc, 2 × 50 mL). The organic layer was washed twice with aqueous NaOH (1 M, 50 mL) and brine (3 × 50 mL) before being dried ( $\text{MgSO}_4$ ). The solvent was removed under vacuum. The crude product was purified by flash chromatography

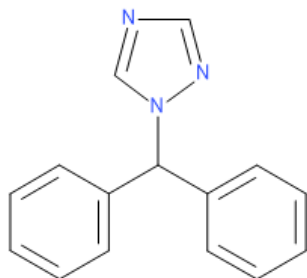
(EtOAc:hexane [1:2]) to give the title compound as an off white solid (0.77 g, 28%);  $^1\text{H}$  NMR (400 MHz,  $\text{CD}_3\text{OD}$ )  $\delta$  (ppm): 8.42 (1H, s, NCHN), 7.87 (1H, s, NCHN), 7.24-7.19 (5H, m, C(Ar)-H), 5.30 (2H, s,  $\text{CH}_2$ );  $^{13}\text{C}\{^1\text{H}\}$  NMR (100.5 MHz,  $\text{CD}_3\text{OD}$ )  $\delta$  (ppm): 152.3, 145.1, 136.8, 129.9, 129.4, 129.1, 54.2; ATR-FTIR  $\nu$  ( $\text{cm}^{-1}$ ): 3126 (CH, m), 3103 (CH, m), 1958-1714 (CH, w, aromatic overtones), 1275 (C=N, s); MS ( $m/z$  - ESI): 91 (BS), 158 ( $\text{M}^+$ ), 159 ( $[\text{M}+\text{H}]^+$ ); RRT: 0.73; mp 60-62 °C [65-67 °C (lit.<sup>81</sup>)].

#### 4-(1H-1,2,4-Triazol-1-ylmethyl)benzonitrile (10d)



4-(1H-1,2,4-Triazol-1-ylmethyl)benzonitrile was obtained from Fluorochem (Glossop, UK) [Batch No. FCB090713] and used without further purification.  $^1\text{H}$  NMR (400 MHz,  $\text{CD}_3\text{OD}$ )  $\delta$  (ppm): 8.50 (1H, s, NCHN), 7.90 (1H, s, NCHN), 7.62 (2H, d, CH), 7.34 (2H, d, CH), 5.42 (2H, s,  $\text{CH}_2$ );  $^{13}\text{C}\{^1\text{H}\}$  NMR (100.5 MHz,  $\text{CD}_3\text{OD}$ )  $\delta$  (ppm): 152.7, 145.5, 142.4, 133.7, 129.8, 119.3, 113.2, 53.4; ATR-FTIR  $\nu$  ( $\text{cm}^{-1}$ ): 3103 (CH, m), 2226 (CN, s), 1750 (CH, w, aromatic overtones), 1275 (C=N, s); MS ( $m/z$  - ESI): 116 (BS), 183 ( $\text{M}^+$ ), 184 ( $[\text{M}+\text{H}]^+$ ); RRT: 0.93; mp 80-84 °C [78-80 °C (lit.<sup>82</sup>)].

### Synthesis of 1-[di(phenyl)methyl]-1H-1,2,4-triazole (10e)



The target compound was prepared using the method reported by Wood *et al.*<sup>80</sup> Diphenylmethanol (1.5 g, 8.22 mmol), 1,2,4-triazole (0.68 g, 9.87 mmol) and *para*-toluenesulphonic acid (0.65 g) were dissolved in dry toluene (100 mL) and heated at reflux equipped with a Dean-Stark trap for 36 h. The reaction mixture was allowed to cool, and the solvent was removed under vacuum. The resulting residue was dissolved in EtOAc (300 mL), washed with 1 M NaOH (2 × 100 mL) and brine (3 × 50 mL), dried (MgSO<sub>4</sub>) and the solvent was removed in vacuo. The crude product was dissolved in hot dry EtOAc (30 mL) and hexane (15 mL) was added dropwise. Upon cooling to room temperature orange crystals were obtained. The crystals were dissolved in minimum amount of EtOAc and purified using Biotage flash chromatography (EtOAc:hexane [1:2]) to give the target compound as orange crystals (1.35 g, 62%); <sup>1</sup>H NMR (400 MHz, CD<sub>3</sub>OD) δ (ppm): 8.02 (1H, s, NCHN), 7.90 (1H, s, NCHN), 7.36 (6H, m, CH), 7.13 (4H, m, CH), 6.76 (1H, s, CH); <sup>13</sup>C{<sup>1</sup>H} NMR (100.5 MHz, CD<sub>3</sub>OD) δ (ppm): 152.0, 144.8, 139.3, 129.4, 129.0, 128.8, 68.1; ATR-FTIR ν (cm<sup>-1</sup>): 3387 (CH, m), 3103 (CH, m), 1963-1769 (CH, w, aromatic overtones), 1445 (CH, m), 1271 (C=N, m); MS (*m/z* - ESI): 167 (BS), 234 (M<sup>+</sup>), 235 ([M+H]<sup>+</sup>); RRT: 1.02; mp 88-89 °C [lit. 89 - 91 °C<sup>83</sup>].

### 3.3 SABRE hyperpolarization - Enhancement calculations

Enhancement factors were calculated using **Equation 2**, where  $|S_{hyp}|$  is the integral of a set region following hyperpolarization and  $|S_{thermal}|$  is the integral of the same set region without hyperpolarization.

$$\text{Equation 2. } \textit{Enhancement} (\varepsilon) = |S_{hyp}| / |S_{thermal}|$$

The same experimental sample was used for the collection of  $|S_{hyp}|$  and  $|S_{thermal}|$ , however,  $|S_{thermal}|$  was allowed to fully relax in the measurement field of 1.4 T, see **Section 3.2**) before data collection. The polarized and reference spectra were collected using identical parameters for comparison reasons. To determine the enhancement level, the raw integrals of the relevant resonances in the polarized and unpolarized spectra were used. To ensure a fair comparison for all samples, each spectrum was properly referenced to the solvent peak and the same chemical shift region was selected for integrals.

#### 3.3.1 SABRE sample preparation

Unless otherwise specified, a sample of ligand (L) was solvated in 600  $\mu\text{L}$  of deuterated methanol with 1.92 mg of the SABRE pre-catalyst,  $[\text{Ir}(\text{IMes})(\text{COD})\text{Cl}]$ . The details of the amounts that were used for this experiment can be seen in **Table 4**. For continuity reasons, the desired concentration for each compound was 0.02 M. The ratio of ligand to pre-catalyst was the same throughout, with four equivalents ligand:pre-catalyst. The sample transferred into a Young's capped NMR tube, followed by vigorous shaking to ensure full ligand and pre-catalyst solvation. The sample was then freeze-thaw degassed, using the procedure that involved submerging the tube in a dry ice and acetone bath, followed by creating a vacuum using a Schlenk line. *Para*-hydrogen was pumped to the capped tube at a pressure of 2.5 bar,

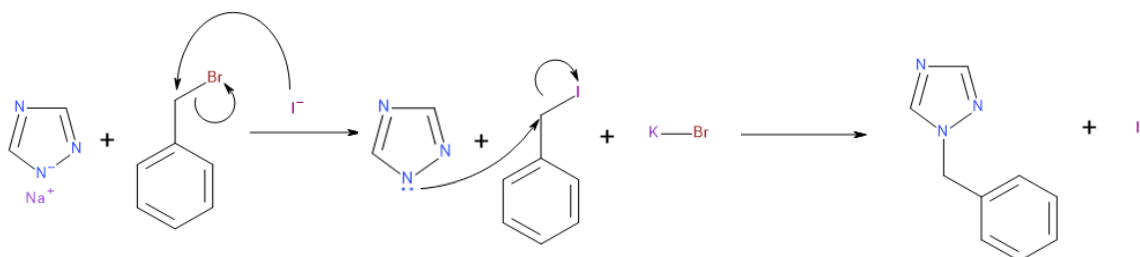
followed by the acquisition of the thermal (Boltzmann) one scan-spectrum using a low-field 60 MHz Oxford Pulsar benchtop NMR instrument. The tube was then shaken for 2 minutes in order to activate the catalyst inside and refilled with *para*-hydrogen, this time increasing the pressure to 3.0 bar. The NMR tube was shaken vigorously for 10 seconds in earth's magnetic field in the vertical plane. After 10 seconds the tube was immediately transferred to the spectrometer to collect the  $^1\text{H}$  NMR spectrum. This method has been repeated three times to produce a set of triplicate data. It is important to shake the tube vertically, as the magnetic field reading in vertical direction is around 0.5 G whereas horizontally it is around 0 G. Due to the composition of the tube (liquid at the bottom, gas at the top), this method gives much better mixing of the biphasic components to ensure maximal polarisation transfer. The whole process was repeated, but this time the tubes were shaken inside a coil, which created a magnetic field of 65 G. After shaking for 10 seconds, the tube was immediately transferred to the spectrometer to collect the  $^1\text{H}$  NMR spectrum. This method was again repeated three times to produce a set of triplicate data.

**Table 4.** Quantities used in SABRE studies during this project

Entry	Compound	Quantity (mg)	[Ir(IMes)(COD)Cl] (mg)	Solvent - CD <sub>3</sub> OD (mL)
1	10a	0.83	1.92	0.6
2	10b	0.99	1.92	0.6
3	10c	1.91	1.92	0.6
4	10d	2.21	1.92	0.6
5	10e	2.82	1.92	0.6
6	3	3.42	1.92	0.6

#### 4. Results and Discussion

Six compounds, **10a** - **e** and **3**, were analysed herein. Four compounds were purchased from commercial sources, whereas the remaining two compounds, **10c** and **10e**, were synthesised. The synthetic method for the preparation of **10c** and **10e** is outlined in **Scheme 1** and **Scheme 2** respectively.

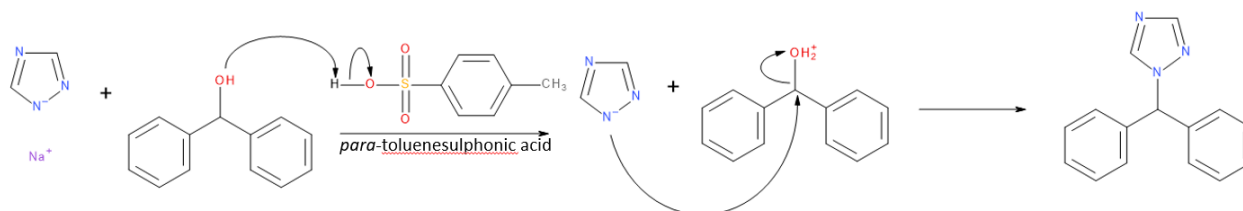


**Scheme 1.** The proposed mechanism for the formation of *N*-benzyltriazole (**10c**).

As seen in **Scheme 1**, **10c** is formed by a S<sub>N</sub>2 reaction between sodium triazole and benzyl bromide. A yield of 28% was obtained which is lower than that reported by Schwärzer *et al.* (50%).<sup>84</sup> The starting materials were dissolved in acetone to ensure all the reactive species are able to interact, allowing the triazole to undergo nucleophilic attack of benzyl bromide. The solvent played a significant role in the reaction. Using acetone as the solvent raises the reactivity of the nucleophile, due to its lack of hydrogen-bond donating capability. Acetone does not form hydrogen bonds with the anionic nucleophile, which means there is a relatively weak interaction between the aprotic solvent and the nucleophile. The treatment of benzyl bromide with an alkali metal halide (in this case potassium iodide, KI) leads to replacement of the halogen *via* a S<sub>N</sub>2 reaction, as explained by the Finkelstein Reaction.<sup>85</sup> This is achieved by an equilibrium process, where the driving force for the reaction is the solubility of salts (KI) and the presence of acetone which shifts the equilibrium of the reaction. The substitution of

bromide in benzyl bromide with iodide in acetone leads to the desired iodide product, since potassium bromide is insoluble in acetone and, therefore, is consequently removed from the equilibrium equation, causing the reaction to shift towards the products. Iodine is a much better leaving group than bromine, because iodine is bigger, therefore C-I is longer and that makes it weaker.<sup>86</sup> Therefore, in the second step of the reaction the newly formed C-I bond can be easily broken, and the iodide will be replaced by a far weaker nucleophile, triazole. During this step, iodide is regenerated, and the cycle starts again.

**Scheme 2** shows the reaction mechanism for the formation of **10e**. The yield, as reported by Doiron *et al.* is 51%.<sup>83</sup> This compares well to the 62% yield obtained herein. The starting materials were dissolved in acetone to ensure all the reactive species were able to interact, allowing the triazole for nucleophilic attack. This involves the protonation of the -OH group by the *para*-toluenesulphonic acid, which results in the creation of an R-OH<sub>2</sub><sup>+</sup> moiety. The triazole nucleophile then attacks the diphenylmethanol ion and the moiety is activated, and thus bond-forming and bond-breaking occur simultaneously, releasing water, a weak base, as a leaving group, forming **10e**.<sup>87</sup>



**Scheme 2.** The proposed reaction mechanism for the formation of **10e**.

#### 4.1 Retention times ( $R_t$ )

Retention time ( $R_t$ ) is a measure of the time taken for a solute to pass through a chromatography column. The longer retention time depends on the interaction of the analyte with the stationary phase. **Table 5** shows the retention times and the relative retention time of molecules **10c - e** and **3** (**entries 1, 2, 4 and 5**). The reference for the relative retention time was the internal standard, eicosane, which eluted at 7.220 min. Compounds **10a** and **10b** were not detected by this methodology; a likely reason for this observation is that the molecules have broken down in the oven due to the heat, and never reached the detector. As seen in the **Table 5**, the retention time increases every time the molecule gets more polar. Retention time is affected by many factors, including the carrier gas flow rate, column length, column temperature and the amount of material injected. All these factors remained the same, in order to make the results comparable. The changing factors were the vapour pressure, which varies depending on the boiling point of the molecule and the polarity of the samples. The lower the boiling point is, the higher the vapour pressure of the compound, meaning the compound will spend more time in the gas phase with very few interactions with the stationary phase, shortening the retention time. The retention time increases if the polarity of the compound and the stationary phase are similar because the interactions between the two are stronger. The stronger the interaction is, the more time it takes to migrate through the column, due to longer interactions of the compound with the stationary phase. The size is also known to affect the retention time because generally, the greater the molecular weight of a compound, the lower its volatility. As expected, the retention time, as well as the relative retention time increases as molecules become bigger, due to the increase of their boiling point and column interactions causing the molecule to stay inside the column for a longer period of time before reaching the GC-MS detector.

**Table 5.** GC-MS retention times of molecules **10c - e** and **3**

Entry	Molecule	Retention Time (min)	Relative retention time (RRT)
<b>1</b>	<b>10c</b>	5.27	0.73
<b>2</b>	<b>10d</b>	6.72	0.93
<b>3</b>	<b>Eicosane</b> (internal standard)	7.22	1.00
<b>4</b>	<b>10e</b>	7.40	1.02
<b>5</b>	<b>3</b>	10.18	1.41

#### 4.2. Mass spectra

On top of the retention times, GC-MS allowed for characterisation of the four compounds **10c - e** and **3** by analysing their mass spectra. The mass spectrum provides two key concepts for each molecule: base peak and parent ion peak. The parent ion peak, which is also called the molecular ion peak, represents the mass of the original molecule. The base peak represents the most abundant component and is the largest peak in the spectrum. The base peak is almost always the most stable ion in the mixture. The mass spectrum of **10c** (**Figure A6** in the appendix) shows a peak at  $m/z$  159, which is the molecular ion peak and a base peak at  $m/z$  91, which is likely to be a benzyl carbocation (tropylium ion). The mass spectrum of **10d** (**Figure A9** in the appendix) has a visible peak at  $m/z$  184, which is responsible for the **10d** molecular ion, and a base peak visible at  $m/z$  116 that is the 4-cyanobenzyl carbocation. The mass spectrum of **10e** (**Figure A12** in the appendix) has a visible molecular ion peak at  $m/z$  235, and a base peak at  $m/z$  167, which would represent the diphenylmethyl ion. The

spectrum on **3** (Figure 8) has a molecular ion at  $m/z$  258 and a base peak visible at  $m/z$  which represents the 4,4'-dicyanodiphenylmethane (Table 6).

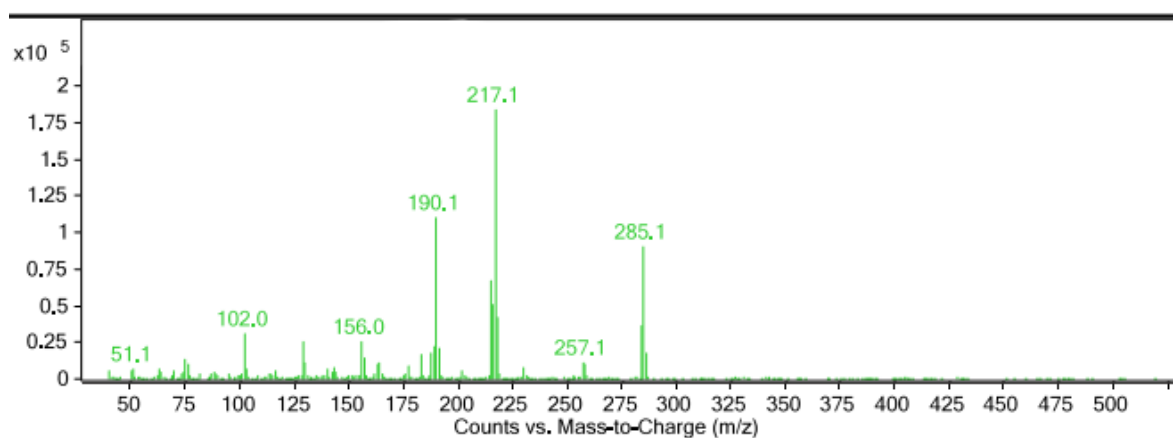


**Figure 8.** GC-MS spectrum of **3** with visible molecular ion and base peaks as well as the corresponding structures of fragments

**Table 6.** Table showing mass/charge values and the structures responsible for the peaks

$m/z$	Molecule
285	
217	

### 4.3 Infrared Spectroscopy (IR)

Infrared Spectroscopy (IR) was the second analytical method which was used for characterisation of synthesised and purchased compounds. IR is the analysis of infrared light interacting with a molecule. Infrared light is part of the electromagnetic radiation span. The radiation extends from the nominal red edge of the visible spectrum at the wavelength range

of 750 nm–100  $\mu\text{m}$ . This range of wavelengths corresponds to a frequency range of 430 terahertz (THz) to 300 gigahertz (GHz).<sup>88</sup> In this report, IR was used to determine the functional groups in molecules based on their frequency (wavenumber). IR spectroscopy measures the vibrations of atoms allowing to determine the functional groups present in a sample. After passing infrared light through a sample, an infrared spectrum is obtained with peaks corresponding to the frequency of absorbed radiation. Each group of bonds have their characteristic vibrational frequencies, allowing the characterisation of a molecule. The measurement obtained is an infrared spectrum, which is a plot of measured infrared intensity versus wavenumber. **Figure 9** and **Figure 10** show IR spectra of molecules **10c** and **3** respectively.

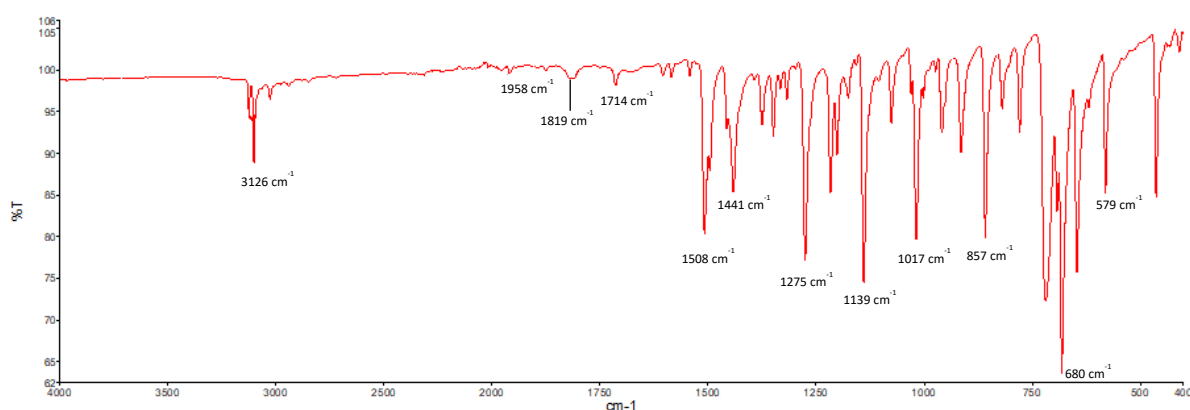


**Figure 9.** IR spectrum of **10c**

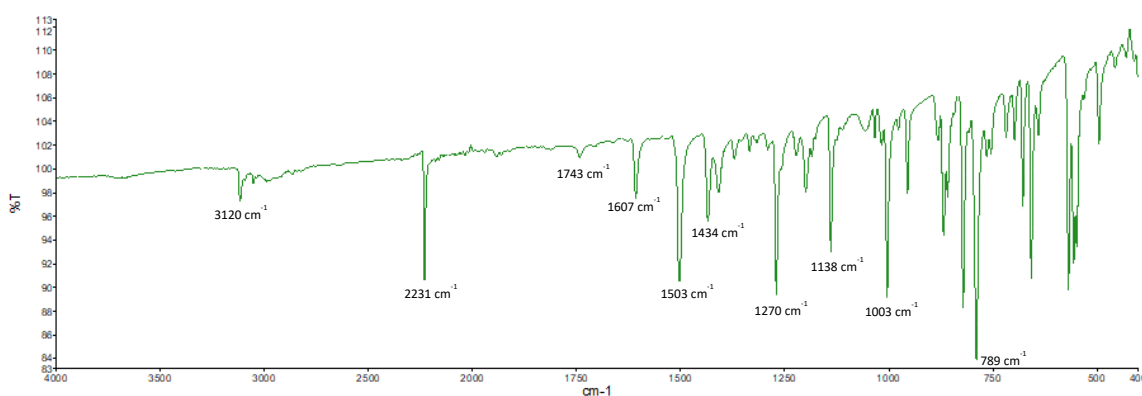


**Figure 10.** IR spectrum of **3**

At first glance, the two figures are similar. Both **Figure 9** and **Figure 10** contain medium C-H stretching peaks at 3126 and 3120  $\text{cm}^{-1}$  respectively, as well as 690–900  $\text{cm}^{-1}$  for out-of-plane C-H bending. Weak aromatic overtones are visible on both spectra in the 1958–1714  $\text{cm}^{-1}$  regions, which indicate the presence of the benzene rings on both molecules. Both figures also contain a carbon-nitrogen double bond peak, at 1275  $\text{cm}^{-1}$  in both cases, which is a part of the triazole ring. The only difference between the two figures, is the strong nitrile functional group peak, which can be seen in **Figure 10** at 2231  $\text{cm}^{-1}$  for  $\text{C} \equiv \text{N}$  stretching. This peak is absent from **Figure 9**. The same nitrile functional group peak is present when the spectrum of **10d** is interrogated (**Figure A8** in the appendix), which is absent from all the other collected spectra (**Figure A1, A3, A11** in the appendix). Spectra collected by Hayat *et al.*<sup>74</sup> for sample **10c** gives near identical wavenumber values to the ones acquired in this report. The same can be said about the collected results for **3**, which were compared to the reported values by Elzoghby *et al.*<sup>89</sup> that proved to be highly similar. These findings further validate the successful characterisation of both compounds.

#### 4.4 High Field $^1\text{H}$ NMR

High-field  $^1\text{H}$  NMR spectra were collected for all the compounds analysed. When comparing the collected data to literature, there are near negligible differences in peak values. According to a report by Kumar *et al.*<sup>90</sup> the chemical shift for NCHN peak of synthesized **10a** appeared at 8.32 ppm in the  $^1\text{H}$  NMR spectrum, which compares well to the commercially purchased sample, in which the peak appeared at a chemical shift of 8.10 ppm (**Figure 11**). The same minor differences in chemical shifts can be seen throughout most of the spectra. Suman *et al.*<sup>91</sup> has reported the chemical shifts of the two NCHN peaks on synthesized **3** to be  $\delta$ 8.09 and

8.71. These chemical shifts are the only ones which appear to be significantly lower when compared to the chemical shifts of the same peaks from a commercially acquired **3**. As seen in **Table 7**, the chemical shift of  $^1\text{H}$ , s, NCHN and  $^1\text{H}$ , s, NCHN were 8.50 and 7.99 ppm respectively (**Figure 12**). It is likely, that the change in chemical shifts was an effect of the use of different solvents as well as different NMR machines. As reported by Dracinsky<sup>92</sup>, different solvents have an effect on the chemical environments such as magnetic shielding and indirect spin-spin coupling constants, therefore changing the chemical shifts.

The reason for focusing primarily on the NCHN peaks is because these peaks are the focus point of hyperpolarization in this report.

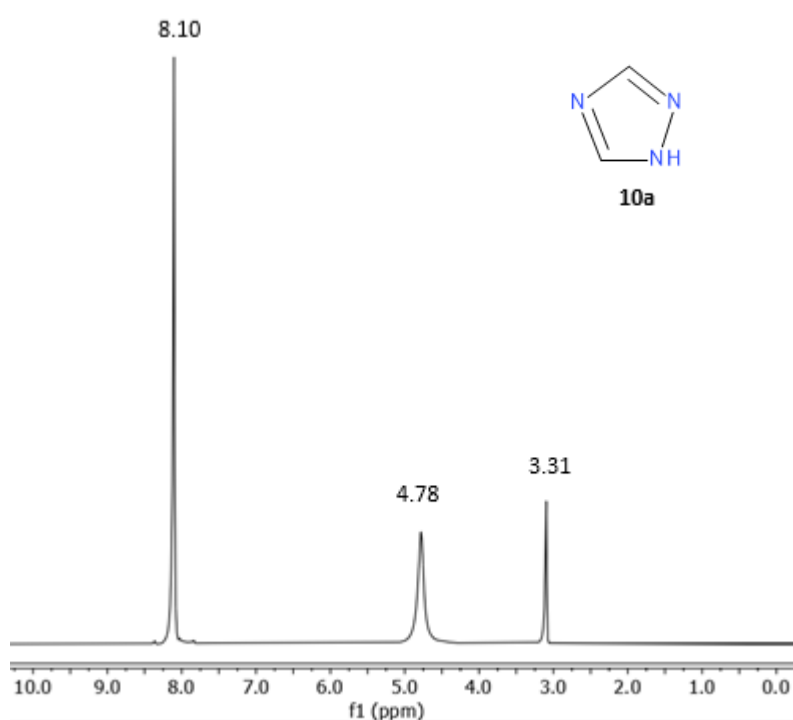


**Figure 11.**  $^1\text{H}$  NMR spectrum **10a** collected in methanol- $\text{d}_4$  (solvent peaks present at the chemical shifts  $\delta$  4.78ppm and 3.31ppm)

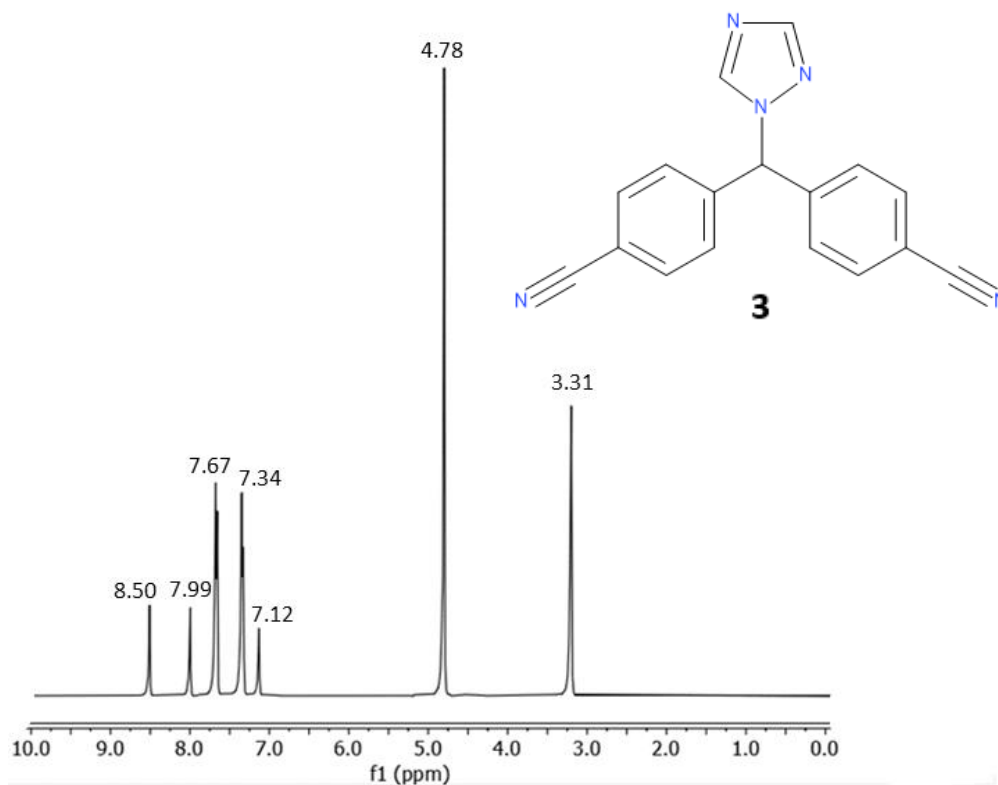


**Figure 12.**  $^1\text{H}$  NMR spectrum of **3** collected in methanol- $\text{d}_4$  (solvent peaks present at the chemical shifts  $\delta$  4.78ppm and 3.31ppm)

It is widely known that structural changes and almost any genuine binding interaction will affect the very sensitive chemical shift. **Table 7** shows the change in chemical shift as the size of the molecule increases. Only the peaks on the 1,2,4-triazole group were focused on due to these peaks being the focus of the SABRE study (**Section 4.7**). The two hydrogens responsible for the peaks of interest,  $\text{H}_\text{A}$  and  $\text{H}_\text{B}$ , are highlighted in **Figure 13**.

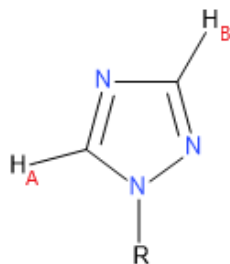


**Figure 13.** Drawing of the 1,2,4-triazole functional group with highlighted H<sub>A</sub> and H<sub>B</sub> atoms for easier distinction between the two protons.

**Table 7.** Table of selected chemical shift values for molecules of interest.

Molecule:	Chemical shift $\delta$ (ppm):	
<b>10a</b>	8.10 (2H, s, NCHN )	
<b>10b</b>	8.27 (1H, s, H <sub>A</sub> )	7.10 (1H, s, H <sub>B</sub> )
<b>10c</b>	8.42 (1H, s, H <sub>A</sub> )	7.87 (1H, s, H <sub>B</sub> )
<b>10d</b>	8.50 (1H, s, H <sub>A</sub> )	7.90 (1H, s, H <sub>B</sub> )
<b>10e</b>	8.25 (1H, s, H <sub>A</sub> )	7.95 (1H, s, H <sub>B</sub> )
<b>3</b>	8.50 (1H, s, H <sub>A</sub> )	7.99 (1H, s, H <sub>B</sub> )

**Table 7** shows small, regular chemical shift changes throughout the table, with values increasing steadily more downfield from **10a** to **10d**. The distinctive pattern for a substituted **10a** is the pair of singlets, visible in molecules **10b - e** and **3**. There is a clear difference in chemical shift between peaks in each molecule. As the molecules get more complex, the difference in chemical shift between the molecules gets smaller. H<sub>A</sub> on carbon 5 and H<sub>B</sub> on carbon 3 on the 1,2,4-triazole ring are split into two peaks for molecule **10b**, and onwards, due to the symmetry being broken by the addition of functional groups. The protons are no longer magnetically equivalent, hence two peaks can be seen. The chemical shift values for **10c** have increased when compared to **10b** due to the addition of the aromatic ring. The protons on the aromatic ring are shifted downfield. This is due to the electrons on the aromatic ring being free to circulate, rather than being fixed in place in bonds which causes

aromatic ring current, that dramatically influences the chemical shifts. The free-flowing electrons in aromatic rings are part of the  $\pi$  electron system, which interact more strongly to the magnetic field with the applied magnetic field and begin to circulate. As a result of this, the nearby protons will experience 3 fields: the shielding field, the applied field, and the field due to the  $\pi$  system. This causes a notable chemical shift change between molecules **10d** and **10e**.

Molecule **10d** has the chemical shift value of 8.50 ppm for  $H_A$ , but molecule **10e** has the chemical shift value of 8.25 ppm. The key difference between these molecules is the addition of a second aromatic group and the absence of the nitrile group on molecule **10e**, as electron density around the proton heavily influences the chemical shift. **10d** has an electronegative nitrile group, which decreases the electron density, causing the proton to be less shielded, which in turn increases the chemical shift.

Molecule **10e** undergoes a non-uniform magnetic field, or anisotropy, which causes the frequency of the absorption to change, causing electrons in **10e** to become shielded, decreasing the chemical shift. Another example of the effect of the electromagnetic nitrile group can be seen in molecules **10c** and **10d**. The only difference between these molecules is the nitrile group, which is absent from **10c**. The electron density is deshielding the protons on **10d**, which causes the small difference in chemical shift; 8.42 and 7.87 ppm compared to 8.50 and 7.90 ppm for **10c** and **10d** respectively. These minor changes help with understanding how the hyperpolarized peaks will form, and where on the spectrum they will appear, based on the complexity of the molecules.

#### 4.5 Low-field $^1\text{H}$ NMR

All molecules **10a - e** and **3** have been characterised using  $^1\text{H}$  bench-top NMR (**Figure 14**). Each signal can be assigned to its corresponding hydrogen environment. When comparing the bench-top spectra to the high field  $^1\text{H}$  NMR (**Figure 15A** and **15B**), the resolution suffers greatly with signals in **Figure 15B** appearing broader and less sharp. On the contrary, bench-top NMR's time efficient procedures, the ease of use and portability outweigh the small setbacks. Signals are present in the aromatic region for **10a - e** and **3**, due to phenyl groups being present. The peaks of interest are located at  $\delta \sim 8.6$  for proton  $\text{H}_\text{A}$  and  $\sim 8.0$  for proton  $\text{H}_\text{B}$  (marked with  $\blacklozenge$  for  $\text{H}_\text{A}$  and  $\blacklozenge$  for  $\text{H}_\text{B}$ , seen **Figure 14**). These represent the hydrogens present on the triazole ring, which will undergo hyperpolarization, as these are closest to the nitrogen donor atoms. The position of nitrogen on the triazole, as well as the functional group attached to N1, breaks the symmetry, causing two environments to appear. These environments are not visible for **10a** due to the molecule being symmetric.  $^1\text{H}$  NMR spectra for **10d** and **3** have visible aromatic multiplets at ca. 7.5 ppm. Spectra for **10c** and **10e** have what appears to be a singlet in that region. This is caused by the absence of the nitrile group on the **10c** and **10e** phenyl ring(s), which break the symmetry of **10d** and **3**. The cause of this single peak is simply due to the use of low field 60 MHz NMR instrument. The weaker magnet produces spectra that is not as resolved compared to its more powerful counterpart, which can be seen in **Figure 15A**. The difference in resolution is roughly a factor of 7, which is why the quality of the spectrum B is much lower than that of A, with peaks appearing closer together and harder to recognise. For example, the extra signal seen in spectrum B is due to the coupling being much larger in the 60 MHz bench-top spectrum compared to the 400 MHz high-field spectrum. Despite this, the distinct hydrogen region is easily identifiable, allowing for the calculation of  $T_1$  values.

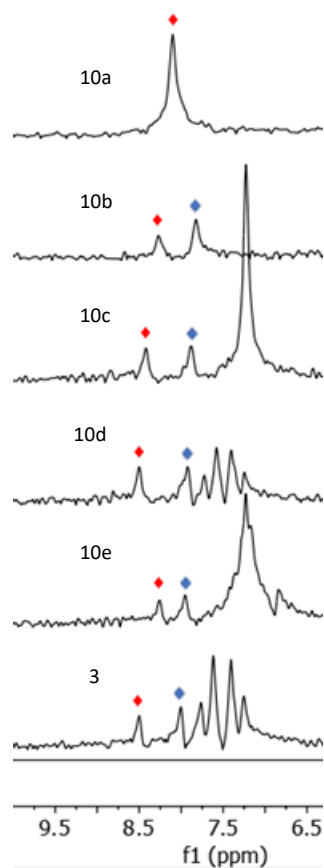


**Figure 14.** Low-field  $^1\text{H}$  NMR spectra of compounds **10a** - **e** and **3**, with highlighted peaks of interest. (marked with  $\blacklozenge$  for  $\text{H}_\text{A}$  and  $\blacklozenge$  for  $\text{H}_\text{B}$ ).

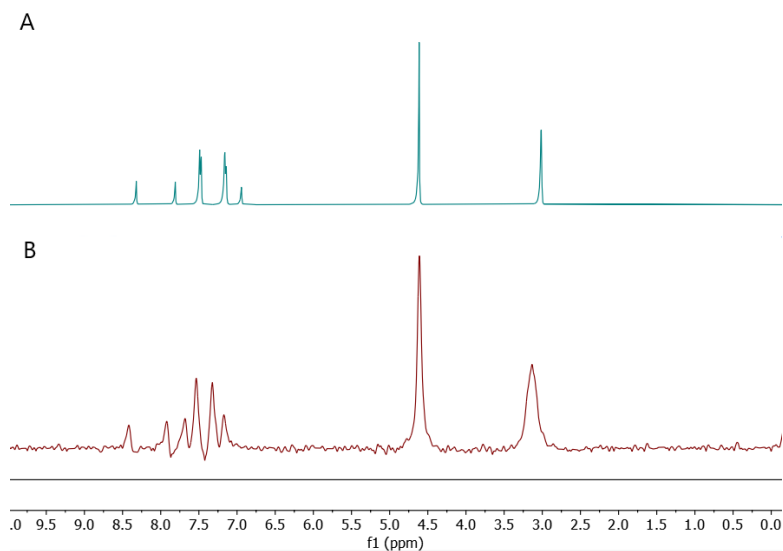


**Figure 15.**  $^1\text{H}$  NMR spectra of the same molecule (**3**) taken on two different NMR instruments. Spectrum A has been acquired on a 400 MHz  $^1\text{H}$  NMR (high field) instrument. Spectrum B has been acquired on a 59.8 MHz  $^1\text{H}$  NMR (bench-top) instrument.

#### 4.6 $^{13}\text{C}\{^1\text{H}\}$ NMR

$^{13}\text{C}\{^1\text{H}\}$  NMR spectra were collected for all the compounds analysed. Just as  $^1\text{H}$  NMR identifies hydrogen atoms,  $^{13}\text{C}\{^1\text{H}\}$  NMR allows the identification of carbon atoms in an organic molecule. The reason for  $^{13}\text{C}$  NMR to only detect the  $^{13}\text{C}$  isotope of carbon, whose natural abundance is only 1.1%, is because  $^{12}\text{C}$ , the main carbon isotope, is not detectable by NMR since it has a spin quantum number of zero and so is not magnetically active. This causes  $^{13}\text{C}$  NMR to be less sensitive to carbon than its proton counterpart, because only a few  $^{13}\text{C}$  nuclei present resonate in the NMR magnetic field.<sup>93</sup> Similarly to high-field  $^1\text{H}$  NMR, there were very minor differences in peak chemical shift when comparing the  $^{13}\text{C}\{^1\text{H}\}$  NMR collected data to literature. The spectroscopic data collected in this report for **10e** is in agreement with that previously reported by Doiron *et al.*<sup>83</sup> The chemical shifts for both molecules are very similar, varying by 0.5 to 2 ppm. **Figure 16** shows a  $^{13}\text{C}$  NMR spectrum **3**, with reported peaks being the same or nearly the same as the peaks reported by Zhang *et al.*<sup>94</sup>

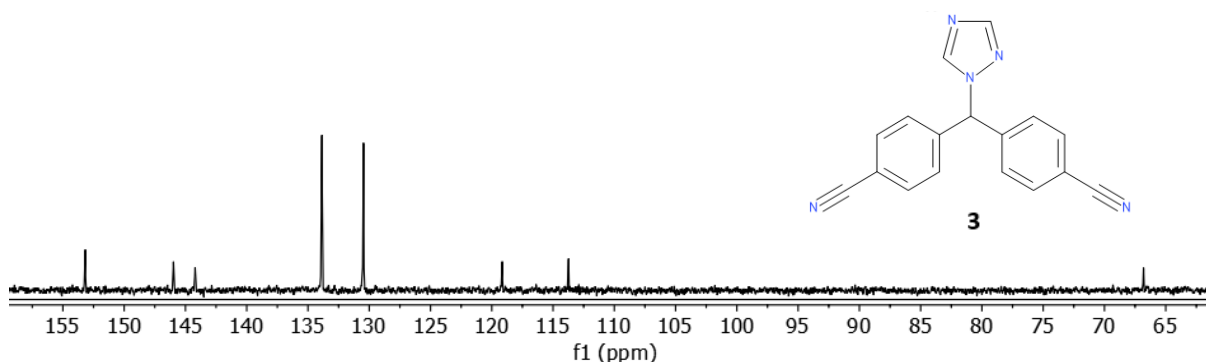


**Figure 16.**  $^{13}\text{C}$  NMR spectrum **3** chemical shift  $\delta$  (ppm): 153.17, 145.98, 144.21, 133.86, 130.47, 199.15, 133.73, 66.81; collected in methanol- $d_4$  (solvent peak present at the chemical shift  $\delta$  49.15 ppm)

#### 4.7 Relaxation times of 10a - e and 3

The spin-lattice relaxation time ( $T_1$ ) was measured for compounds **10a - e** and **3** in order to understand how the structural complexity affects the relaxation time. When a  $90^\circ$  radio frequency pulse is applied, the longitudinal magnetisation ( $M_z$ ) will be flipped towards the  $xy$  plane. The signal detector in NMR is positioned along the  $xy$  plane, so the intensity of the detected signal will decrease over time due to  $z$ -axis relaxation.<sup>62</sup> In this report the longitudinal (spin-lattice) relaxation,  $T_1$ , was measured. The relaxation can be represented mathematically as:

$$\text{Equation 3. } M_{z(t)} = M_{z(0)}(1 - 2e^{-\frac{t}{T_1}})$$

The experiment consisted of a series of measurements, each with an increasing time delay ( $\tau$ ). In terms of the pulses applied, the  $T_1$  pulse sequence utilised begins with a  $180^\circ$  pulse to flip  $M_z$  to  $M_{-z}$ . Prior to a  $90^\circ$  pulse to flip magnetisation into the transverse plane, a time delay of length  $\tau$  is applied. At short  $\tau$ , the magnetisation signal when flipped into the transverse plane will begin from  $M_{-z}$  whereas at longer values of  $\tau$ , relaxation will have occurred so that magnetisation will have been partly, or fully, restored in to the  $M_z$  direction. A plot of signal intensity as a function of  $\tau$  can then be plotted; a representative  $T_1$  plot is shown in **Figure 17**. The  $T_1$  value can then be calculated from this. It is important to know the  $T_1$  value of each compound, as 5-6  $T_1$  are required for the maximum amount of equilibrium magnetisation ( $M_z$ ) to be restored.<sup>64</sup> Furthermore,  $T_1$  is a measure of how long a hyperpolarized state will persist for; this is an important consideration for biological applications.

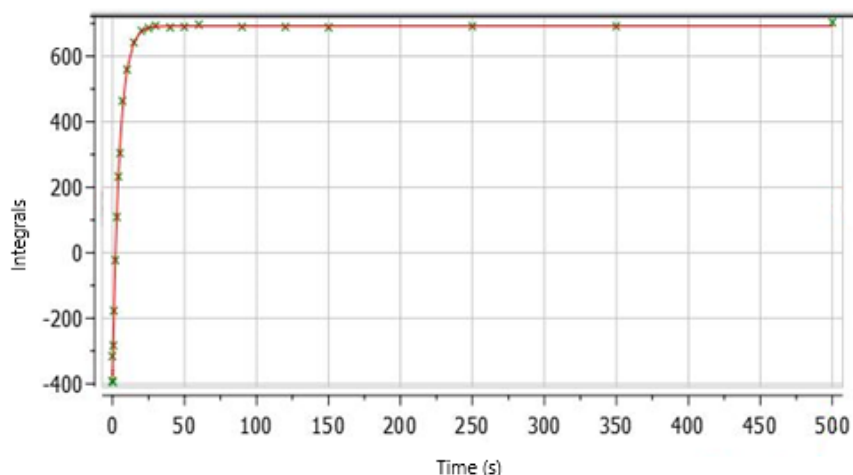


**Figure 17.** A graph with time (s) on x-axis and integrals on y-axis with a plotted curve used to calculate the relaxation time ( $T_1$ ) of molecule **10a**.

$T_1$  values were calculated for **10a - e** and **3** in the presence and absence of the SABRE pre-catalyst, [Ir(IMes)(COD)Cl], and either in an atmosphere of air or vacuum (**Table 8**). All data was collected in  $d_4$ -MeOH.

**Table 8.**  $T_1$  values of samples **10a - e** and **3** with and without the presence of the catalyst

Entry	Compound	Without the catalyst		With the catalyst	
		$T_1$ in air / s	$T_1$ in vacuum / s	$T_1$ in air / s	$T_1$ in vacuum / s
1	10a	6.3	44.8	6.2	41.1
2	10b	5.8	24.3	4.5	31.6
3	10c	5.0	17.2	4.3	27.3
4	10d	5.3	12.0	4.7	25.5
5	10e	2.8	19.9	4.1	13.5
6	3	2.8	17.1	3.5	10.1

The relaxation times in air are much smaller due to the presence of oxygen. Dobzhenetskiy *et al.*<sup>95</sup> reported that paramagnetic complexes shorten the  $T_1$  time. Oxygen is a paramagnetic molecule, which means it affects the relaxation times as the unpaired electrons have a high magnetic moment, which promotes relaxation and in turn, shortens  $T_1$ . Therefore, the relaxation times for samples in vacuum are 7 to 10 times longer, as there is no oxygen present.

The same results were reported by Ashworth *et al.*,<sup>96</sup> who compared the difference in  $T_1$  relaxation times between pyridine samples in air and in vacuum. It was found that  $T_1$  calculated in air to be 4.8 s, and 25.1 s in vacuum – 5 times longer. This reflects the data found in this report, where the  $T_1$  for compound **10a (entry 1)**, which is of similar size to pyridine, is also around 5 times longer in vacuum. Similarly, to the results recorded for **10a** without the catalyst, the relaxation time with catalyst and in vacuum is 7 times longer when compared to its air counterpart. But upon closer examination of the relaxation values, it was noted that the observed  $T_1$  values (**entries 1-6**) in air and in vacuum become shorter between samples after the catalyst has been introduced. For molecule **3 (entry 6)** the relaxation time in vacuum is only 3 times longer in comparison to the  $T_1$  time taken in air, which suggests the presence of the catalyst decreases the time it takes for the molecule to go back into its original relaxation state. During SABRE, rapid polarization transfer is beneficial, but without *para*-hydrogen, the catalyst lowers the hyperpolarization by reducing  $T_1$ . **Table 8** shows, the values for  $T_1$  were becoming shorter, as the size of the molecules increased. Medium-sized molecules are known to have slower tumbling rates – which affect the spin-lattice relaxation time - when compared to small and large molecules.<sup>97</sup> As represented in **Figure 18**, “free” water – shown on the right, with its small molecule size is tumbling too fast in its free state to be effective at  $T_1$  relaxation. Large molecules, as well as molecules in solid states tumble too slowly, again increasing the relaxation time. Medium molecules, located closest to the Larmor frequency ( $f_0$ ), have the most optimal tumbling rate, therefore having the shortest  $T_1$ .  $f_0$  is the rate of

precession of the magnetic moment of the proton around the external magnetic field, which is related to the strength of the magnetic field

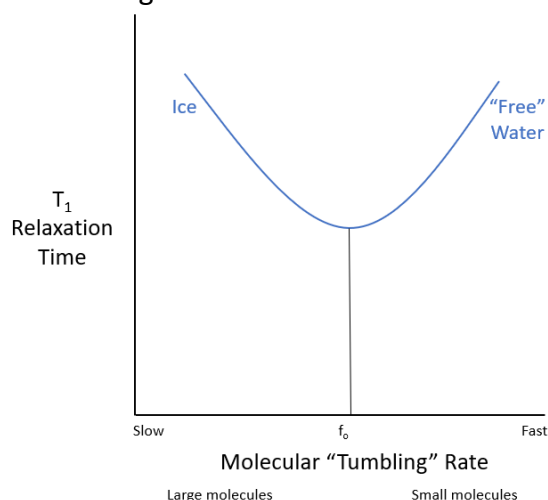


**Figure 18.** A graph representing the difference in  $T_1$  relaxation time based on the speed of molecular tumbling.

Molecules closest to the  $f_0$  give the most efficient  $T_1$  relaxation times. Hence, when applying this theory to molecules **10a - e** and **3**, **10a** has a longer  $T_1$  due to its smaller size when compared to molecules **10b - e** and **3**. **3** has the shortest  $T_1$  time due to it being a medium sized molecule, which lies closer to  $f_0$ , therefore having a slower tumbling rate.

The data which was collected in this report is representative of the data disclosed previously.  $T_1$  data reported by Weinert<sup>98</sup> shows data for propanol-substituted germanium to be 1.2 s, and for pure germanium to be 10.6 s, which are similar to the previously reported **10a** and **3** values (**entries 1** and **6**). The larger molecule has a much smaller spin-lattice relaxation time in comparison to the smaller molecule. These values are another example of how a bigger molecule has a lower  $T_1$  value, and the smaller molecule has a larger  $T_1$  value due to the difference in their tumbling rate.

## 4.8 Hyperpolarization

Hyperpolarization makes ordinarily impractical measurements become possible, because it turns typically weak NMR and MRI responses into strong signals. This section shows how compounds **10a**, **10b**, **10c**, **10d** and **3** react to hyperpolarization in two different magnetic fields; 0.5 G – the earth's magnetic field and 65 G – the optimal magnetic field strength for SABRE hyperpolarization, according to Zeng *et al.*<sup>99</sup>

To understand how/if the complexity of a molecule affects hyperpolarization, a series of experiments were performed on molecules **10a - d** and **3**. All molecules have a triazole ring, which should be able to bind to the Ir catalyst through the nitrogen situated in the second and fourth position of the ring. The prediction that molecules **10a - d** and **3** would hyperpolarize was based on the fact that, according to literature, pyridine shows enhancements of over 1000.<sup>74</sup> The triazole group on molecules **10a - d** and **3** is not hindered by any of the other groups, and therefore allowed most of the magnetisation to be propagated from the *para*-hydrogen derived hydride ligands through to the triazole protons. It has been reported that hyperpolarization using SABRE method is not limited to protons, and that hyperpolarization can be transferred to <sup>13</sup>C and <sup>15</sup>N.<sup>100</sup> Literature has shown that SABRE hyperpolarization is mostly performed on compounds containing nitrogen. Letrozole has been picked as a drug of interest, due to its potential to hyperpolarize and if successful, the future implications. It is understood that nitrogen can be hyperpolarized due to the existence of a free orbital on the atom, giving <sup>15</sup>N a 1/2 spin which allows for the polarization transfer. The free orbital on <sup>15</sup>N binds to the protons without posing a steric barrier once hyperpolarized, and by providing an extended time window for the utilization of the hyperpolarized compounds, it can potentially retain their spin alignment for tens of

minutes.<sup>74,101</sup> This information indicates that molecules containing the nitrile group, such as 10d and 3 have more than one way of binding with the catalyst, due to the existence of a free orbital on the additional N atom which is capable of interacting with a metal centre, as reported by R. Mewis *et al.*<sup>102</sup> As such, studying the <sup>15</sup>N SABRE polarization could be an area of potential future research, but this approach typically requires compounds to be <sup>15</sup>N-labelled.

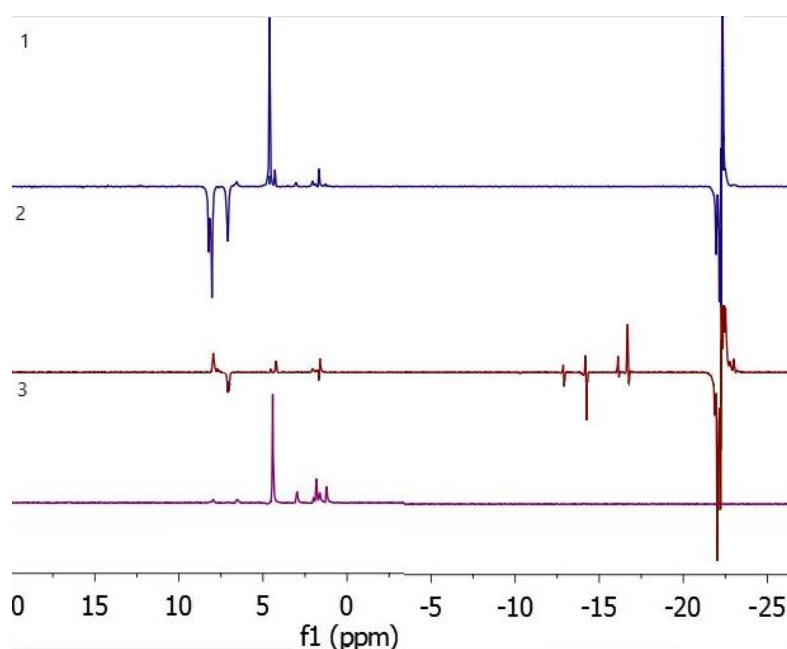


**Figure 19.** <sup>1</sup>H NMR SABRE spectra for **10a**. (1) taken after *para*-hydrogen addition at 65 G, (2) taken after *para*-hydrogen addition at 0.5 G, (3) thermal spectrum.

The hydride intermediates observed in spectrum 2 between delta -10 to -20 in **Figure 19**, which are absent from spectrum 1 indicate the successful catalyst activation, which means the required J-coupling network was established. The same trend was seen for hyperpolarized spectra for compounds **10a - d** and **3**. In addition to this, the colour of the sample inside the tube turned from vibrant yellow to near colourless, as a result of a change in oxidation state of the iridium catalyst centre. The addition of *para*-hydrogen to the complex means that Ir(I)

is oxidised to Ir(III), through an oxidative addition process, which explains the change in geometry of the catalyst from square planar to octahedral; the complex  $[\text{Ir}(\text{IMes})(\text{L})_3(\text{H})_2]^+$  is proposed to form where  $\text{L} = \mathbf{10a} - \mathbf{d}$  or  $\mathbf{3}$ . Once hydrogenated, the catalyst is fully activated and ready to propagate hyperpolarization efficiently to the substrate. The  $^1\text{H}$  NMR spectra acquired following polarization transfer at 0.5 G and 65 G have an enhancement of 3-fold and 54-fold respectively.

**Figure 20 and 21** show the data collected after SABRE experiment on molecules **10c** and **3**. Similarly to spectrum visible in **Figure 19**, the hydride intermediates are not visible, as well as the colour of the sample inside the tube turned from vibrant yellow to near colourless, suggesting a successful catalyst activation. Peak enhancement level ( $\epsilon$ ) was measured using the integration of a hyperpolarized NMR signal, to its unpolarized (thermal) counterpart. **Figure 20** shows an 8-fold enhancement at 0.5 G, whilst the enhancements almost double to 17-fold following polarization transfer at 65 G (**Figure 20-1**). **Figure 21-1** and **Figure 21-2** shows spectra of hyperpolarized **3** with a peak enhancement of 6-fold and 7-fold respectively, when compared to the thermal spectrum generated before activation of the catalyst.

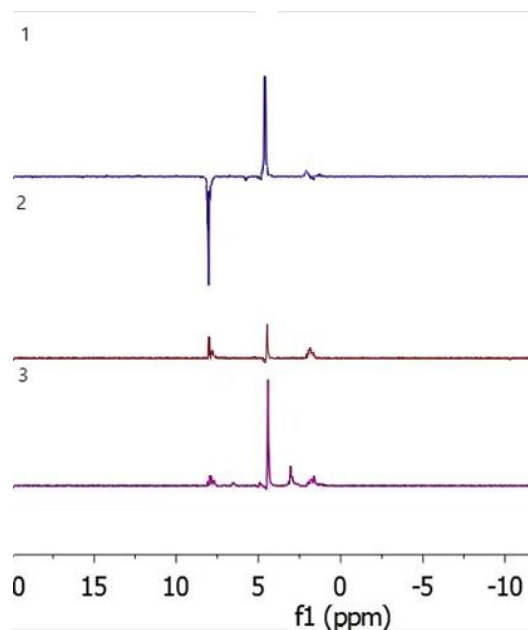


**Figure 20.**  $^1\text{H}$  NMR SABRE spectra for **10c**. (1) taken after *para*-hydrogen addition at 65 G, (2) taken after *para*-hydrogen addition at 0.5 G, (3) thermal spectrum.

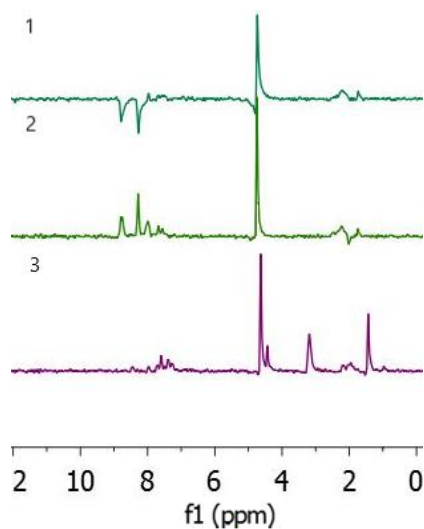


**Figure 21.**  $^1\text{H}$  NMR SABRE spectra for **3**. (1) taken after *para*-hydrogen addition at 65 G, (2) taken after *para*-hydrogen addition at 0.5 G, (3) thermal spectrum.

As seen in **Figures 19-21**, hyperpolarization is evident, shown through the presence of enhanced emission signals at 7.96 ppm. This observation alone shows that the compounds

have successfully hyperpolarized. **Table 9** shows the peak enhancement for each tested molecule.

**Table 9.** Data showing the enhancements of a H<sub>B</sub> peak in different magnetic fields

Entry	Compound	Peak enhancement ( $\epsilon$ ) at the magnetic fields indicated	
		0.5 G	65 G
1	10a	-6	-54
2	10b	-3	-20
3	10c	-8	-17
4	10d	-0.05	-9
5	3	-6	-7

The magnitudes acquired from the data are lower than expected (**Table 9**), especially when compared to molecules like pyridine. In the limited data available in literature for molecules **10a - d** and **3**, it is reported that the peak enhancement is comparable to the data collected in this report. Hermkens *et. al.*<sup>101</sup> report a peak enhancement of 50-fold for molecule **10b** (**entry 2**). The enhancement levels cannot be fully compared due to the equipment limitations encountered during this study. The main differences were the use of different magnetic field strength, as well as a lower percentage of atmospheric *para*-hydrogen. Hermkens used 100% *para*-hydrogen, which is why their reported data is a factor of 3 larger than the data reported in this study. Therefore, a stronger enhancement of molecules could be achieved in this study by using a higher percentage of *para*-hydrogens, which would increase the acquired peak enhancement data by a factor of 3, as well as increasing the pressure of *para*-hydrogen inside the tube from 3 bar to 5 bar. As reported by Rayner *et al.*,<sup>96</sup> increasing the *para*-hydrogen

pressure from 3 to 5.5 bar can boost the value of hyperpolarization from 22% to 41% for a molecule.

Rayner *et al.*<sup>96</sup> also reported that the locations of protons on the ring have a great effect on effective SABRE transfer, and therefore hyperpolarization levels, due to potential isolation from the hydride ligands of the catalyst. It was concluded that most desirable molecular architecture for efficient magnetisation transfer via SABRE is placing a proton next to a nitrogen. Since all *N*-binding sites on compounds **10a - d** and **3** are the same, it was reasonable to assume they should all have the same or similar polarization levels. The experiments proved otherwise, with the peak enhancements mostly decreasing when moving onto the next molecule with a higher molecular mass. **3 (entry 5)** has the peak enhancement of -7, which suggests that the molecule has been polarized successfully, but the enhancement is not very high compared to other entries. Peak enhancement measurements were repeated three times in every magnetic field and only the highest reading has been recorded, as sometimes the catalyst took longer to activate. The poor performance of **3** under SABRE must be a consequence of low  $T_1$  values, when compared to **10a (entry 1)** with high polarization level and a long relaxation time. This trend is visible when comparing  $T_1$  data between molecules in **Table 8**. The relaxation times slowly decrease with the added complexity of the molecule, which reflects the decrease in hyperpolarization level in **Table 9**. The theory, which was assumed prior to undertaking the experiment, appears to be correct. Compound **10e** has not been used in SABRE hyperpolarization due to limited access to the laboratory and the *para*-hydrogen generator. If given the chance, a SABRE hyperpolarization would be carried out on compound **10e** to show how the size of a molecule affects the peak enhancement, and how the produced results would fit into the already generated pattern.

## 5. Conclusion

To conclude, the carried-out work was a pilot study showing molecule **3** can be hyperpolarized, as well as how the size of a molecule affects the peak enhancement. The data, which was collected during hyperpolarization, shows there is some correlation between the size of the molecule, or the functional groups attached, and the peak enhancement ( $\epsilon$ ). The size and functional groups do affect the chemical shift during  $^1\text{H}$  NMR analysis, and the data suggests that the same can be said when SABRE hyperpolarization is being carried out. **10a** produced the largest enhancement of -54 at 65 G, probably due to the similarity to pyridine, but the enhancements were not as high as expected. However, the main goal of this report was to simply demonstrate that the clinically approved drug letrozole could be hyperpolarized via SABRE, to obtain a hyperpolarized  $^1\text{H}$  NMR spectra. Data seen in **Table 9** shows that this aim has been accomplished, with a  $\epsilon$  of 7-fold when a 65 G magnetic field was utilised for polarization transfer. For this report, all of the molecules were dissolved in methanol- $d_4$ , as it was reported to have the best polarization transfer magnetic field strength.<sup>98</sup> Upon the evaluation of the literature, this work would have undoubtedly benefited from better optimisation of the systems investigated. According to Zeng *et al.*,<sup>99</sup> temperature has an effect on the peak enhancement for SABRE hyperpolarization. The 'shake and analyse' technique used in this report gave a potential variance, further increasing the inconsistency of data collection. If the methods were completely unsuccessful, there would be no observable hyperpolarization entirely, so even these non-fully optimised systems show the SABRE hyperpolarization method was successful in that the molecules investigated were polarized. The research contained here has again proven that the hyperpolarization technique, SABRE, can be applied to biologically relevant compounds. This paves the way for future

opportunities that might be focused around studying the biological activity of **3**, coupled with SABRE hyperpolarization towards, for example, MRI applications.

## 6. Future Work

The aim of this report was to revolutionize clinical diagnosis of breast cancer, in terms of utilising the hyperpolarization technique. Proof of concept data has been obtained as it has been proven that letrozole can be hyperpolarized. The experimental work carried out in this report has to be optimised before final conclusions can be drawn. Variables, such as the optimisation of the magnetic field for polarization transfer, *para*-hydrogen pressure, and *para*-hydrogen mole fraction have to be adjusted to show the best conditions for letrozole hyperpolarization. In future work, it would be beneficial to find out how different solvents affect the hyperpolarization of letrozole and its derivatives. Methanol- $d_4$  was chosen as the first test solvent based on the literature, but it is reported by Zeng *et al.*,<sup>99</sup> that it is highly toxic, therefore making it unsuitable for study *in vivo*. Therefore, solvents like ethanol and DMSO, which have lower toxicity and are suitable for intravenous injection (DMSO is often used as a drug vehicle in medical research),<sup>99</sup> would be the next step in assessing letrozole's use as cancer tracing agent. It was also found, that in SABRE, the polarization efficiency depends not only on the magnetic field, but also on the concentration of the substrate. Letrozole is utilised at a dosage of 2.5 mg daily. The mass used for this research was 3.4 mg. Therefore, it would be advised to run SABRE experiments using the daily dosage. This would be advantageous, in terms of collating evidence, to validate whether or not the drug could act as a tracing agent, as well as a medication. In terms of the hyperpolarization itself, it would be prudent to broaden the knowledge of the topic around the size and complexity of the molecule and the affects it has on the hyperpolarization and peak enhancement. Finally, in

terms of the biological view, it would be advisable to see how hyperpolarization affects drugs which are inside living cells. It is widely understood how the MRI instruments work in hospitals, to create images based on the alignment of protons in the body, and how different tissues create different images. So, it would be worthwhile to add a drug which can be  $^1\text{H}$  hyperpolarized and test whether it will be visible under MRI conditions, especially against a strong  $^1\text{H}$  background signal.

## References:

1. L. A. Torre, R. L. Siegel, E. M. Ward, A. Jemal, *Cancer Epidemiology Biomarkers Prevention*, 2016, **25**, 16.
2. Cancer Research UK, <https://www.cancerresearchuk.org/health-professional/cancer-statistics/mortality>, Accessed May 2020.
3. J. R. Benson, I. Jatoi, *Future Oncol.* 2012, **6**, 697-702.
4. N. Harbeck, F. Penault-Llorca, J. Cortes, M. Gnant, N. Houssami, P. Poortmans, K. Ruddy, J. Tsang, F. Cardoso, *Nature Reviews Disease Primers*, 2019, **5**, 66.
5. Z. Momenimovahed, H. Salehiniya, *Dove Med. Press*, 2019, **11**, 151-164.
6. B. A. W. Majeed, I. Javed, T. Khaliq, F. Muhammad, A. Ali, A. Raza, *Asian Pac. J. Cancer Prev.*, 2014, **15**, 3353-3358.
7. Y.-S. Sun, Z. Zhao, Z.-N. Yang, F. Xu, H.-J. Lu, Z.-Y. Zhu, W. Shi, J. Jiang, P.-P. Yao, H.-P. Zhu, *Int. J. Biol. Sci.*, 2017, **13**, 1387-1397.
8. R. L. Siegel, K. D. Miller, A. Jemal, *CA: A Cancer J. Clinicians*, 2017, **67**, 7-30.
9. N. Howlader, A. M. Noone, M. Krapcho, D. Miller, A. Brest, M. Yu, J. Ruhl, Z. Tatalovich, A. Mariotto, D. R. Lewis, H. S. Chen, E. J. Feuer, K. A. Cronin. *SEER Cancer Stat. Rev.*, 1975-2017
10. A. G. Waks, E. P. Winer, *JAMA*, 2019, **321**, 288-300.
11. Y. Feng, M. Spezia, S. Huang, C. Yuan, Z. Zeng, L. Zhang, X. Ji, W. Liu, B. Huang, W. Luo, B. Liu, Y. Lei, S. Du, A. Vuppalapati, H. H. Luu, R. C. Haydon, T.-C. He, G. Ren, *Genes Dis.*, 2018, **5**, 77-106.
12. D. Ghosh, J. Griswold, M. Erman, W. Pangborn, *Nature*, 2009, **457**, 219-223.
13. W. C. Boon, E. R. Simpson, *Handb. Neuroendocrinol.*, 2012, 723-737
14. P. C. White, *Vitam. Horm.*, 1994, **49**, 131-195
15. R. W. Brueggemeier, J. A. Richards, T. A. Petrel, *J. Steroid Biochem. Mol. Biol.*, 2003, **86**, 501-507.
16. F. Ades, K. Tryfonidis, D. Zardavas, *Ecancermedicalscience*, 2017, **11**, 746-746.
17. I. H. Abdulkareem, I. B. Zurmi, *Nigerian J. Clin. Pract.*, 2012, **15**, 9-14
18. J. Li, Z. Wang, Z. Shao, *Cancer Med.*, 2019, **8**, 1943-1957
19. A. E. Wakeling, *Endocr Relat Cancer*, 2000, **7**, 17-28
20. B. Baggett, R. I. Dorfman, L. L. Engel, K. Savard, *J. Biol. Chem.*, 1956, **221**, 931-941.
21. S. Janicki, N. Schupf, *Curr. Neurol. Neurosci. Rep.*, 2010, **10**, 359-66.
22. I. Shiina, M. Suzuki, K. Yokoyama, *Tetrahedron Lett.*, 2004, **45**, 965-967
23. National Center for Biotechnology Information. PubChem Annotation Record for TAMOXIFEN. <https://pubchem.ncbi.nlm.nih.gov/source/hsdb/6782> Accessed May 2020.
24. J.-P. Bégué, D. Bonnet-Delpon, *Fluorine Health*, 2008, **1**, 553-622
25. National Center for Biotechnology Information. PubChem Annotation Record for FULVESTRANT. <https://pubchem.ncbi.nlm.nih.gov/source/hsdb/7658>. Accessed May 2020.
26. M. L. Rao, H. Kölsch, *Psychoneuroendocrinology*, 2003, **28**, 83-96.
27. J. Cui, Y. Shen, R. Li, *Trends Mol. Med.*, 2013, **19**, 197-209
28. M. L. Rao, H. Kölsch, *Psychoneuroendocrinology*, 2003, **28**, 83-96.
29. E. R. Simpson, *J. Steroid Biochem. Mol. Biol.*, 2003, **86**, 225-230.
30. C. J. Fabian, *Int. J. Clin. Pract.*, 2007, **61**, 2051-2063.
31. Y. Hong, R. Rashid, S. Chen, *Steroids*, 2011, **76**, 802-806

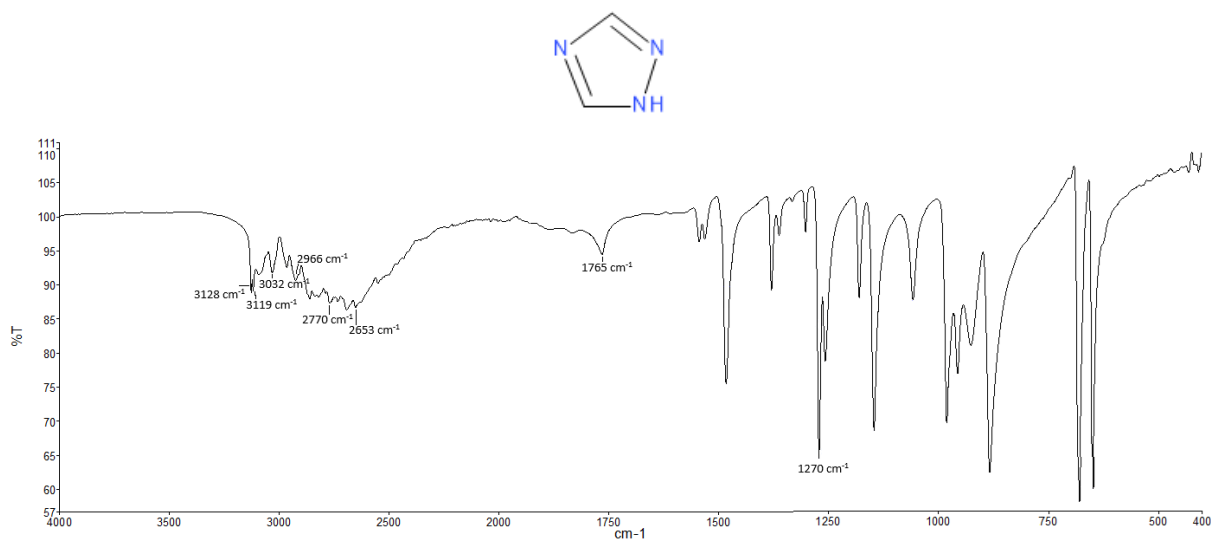
32. L. M. Demers, J. C. Melby, T. E. Wilson, A. Lipton, H. A. Harvey, R. J. Santen, *J. Clin. Endocrinol. Metab.*, 1990, **70**, 1162-1166
33. R. C. Stein, M. Dowsett, J. Davenport, A. Hedley, H. T. Ford, J. C. Gazet, R. C. Coombes, *Cancer Res.*, 1990, **50**, 1381-1384,
34. J. Geisler, *Br. J. Cancer*, 2011, **104**, 1059-1066.
35. J. M. Dixon, L. Renshaw, J. Dixon, J. Thomas, *Breast Cancer Res. Treat.*, 2011, **130**, 871-877
36. W. Eiermann, S. Paepke, J. Appfelstaedt, A. Llombart-Cussac, J. Eremin, J. Vinholes, L. Mauriac, M. Ellis, M. Lassus, H. A. Chaudri-Ross, M. Dugan, M. Borgs, *Ann. Oncol.*, 2001, **12**, 1527-1532.
37. M. J. Ellis, A. Coop, B. Singh, L. Mauriac, A. Llombert-Cussac, F. Jänicke, W. R. Miller, D. B. Evans, M. Dugan, C. Brady, E. Quebe-Fehling, M. Borgs, *J. Clin. Oncol.*, 2001, **19**, 3808-3816.
38. J. Berry, *Clin. Ther.*, 2005, **27**, 1671-1684.
39. J. D. Kaunitz, *Dig. Dis. Sci.*, 2018, **63**, 1100-1101.
40. D. Marion, *Mol. Cell Proteomics*, 2013, **12**, 3006-3025.
41. I. Pelczer, R. Freeman, R. Smith, *Magn. Reson. Chem.*, 2005, **43**, 970
42. D. J. Houde, S. A. Berkowitz, *Biophys. Charact. Proteins Dev. Biopharm.*, 2019, **2**, 586
43. D. A. Pollacco, *Magn. Reson. Imaging*, 2016
44. D. A. Case, *Curr. Opin. Struct. Biol.*, 2013, **23**, 172-176.
45. D. A. Barskiy, A. M. Coffey, P. Nikolaou, D. M. Mikhaylov, B. M. Goodson, R. T. Branca, G. J. Lu, M. G. Shapiro, V.-V. Telkki, V. V. Zhivonitko, I. V. Koptuyug, O. G. Salnikov, K. V. Kovtunov, V. I. Bukhtiyarov, M. S. Rosen, M. J. Barlow, S. Safavi, I. P. Hall, L. Schröder, E. Y. Chekmenev, *Chem.*, 2017, **23**, 725-751.
46. H. Takahashi, C. Fernández de Alba Encinas, D. Lee, V. Maurel, S. Gambarelli, M. Bardet, S. Hediger, A.-L. Barra, G. De Paëpe, *J. Magn. Reson.*, 2013, **239**, 91-99.
47. M. M. Chaumeil, C. Majac, S. M. Ronen, *Methods Enzymol.*, 2015, **561**, 1-71
48. A. S. Edison, F. C. Schroeder, *Compr. Nat. Prod. Chem.*, 2010, **9**, 169-196
49. M. L. Hirsch, N. Kalechofsky, A. Belzer, M. Rosay, J. G. Kempf, *J. Am. Chem. Soc.*, 2015, **137**, 8428-8434.
50. E. Babcock, Z. Salhi, T. Theisselmann, D. Starostin, J. Schmeissner, A. Feoktystov, S. Mattauch, P. Pistel, A. Radulescu, A. Ioffe, *J. Phys.: Conf. Ser.*, 2016, **711**
51. L. Ebner, J. Kammerman, B. Driehuys, M. L. Schiebler, R. V. Cadman, S. B. Fain, *Eur. J. Radiol.*, 2017, **86**, 343-352
52. R. Giernoth, *Mech. Homogeneous Catal.*, 2005, 359-378.
53. Y. Okuno, S. Cavagnero, *J. Phys. Chem.*, 2016, **120**, 715-723.
54. M. Mompeán, R. M. Sánchez-Donoso, A. de la Hoz, V. Saggiomo, A. H. Velders, M. V. Gomez, *Nat. Commun.*, 2018, **9**, 108.
55. M. Irfan, N. Eshuis, P. Spanning, M. Tessari, M. Feiters, F. Rutjes, *J. Phys. Chem. C*, 2014, **118**, 13313-13319.
56. K. V. Kovtunov, E. V. Pokochueva, O. G. Salnikov, S. F. Cousin, D. Kurzbach, B. Vuichoud, S. Jannin, E. Y. Chekmenev, B. M. Goodson, D. A. Barskiy, I. V. Koptuyug, *Phys. Chem. Chem. Phys.*, 2019, **21**, 26477-26482
57. M. L. Truong, T. Theis, A. M. Coffey, R. V. Shchepin, K. W. Waddell, F. Shi, B. M. Goodson, W. S. Warren, E. Y. Chekmenev, *J. Phys. Chem. Nanomater Interfaces*, 2015, **119**, 8786-8797.

58. P. Nikolaou, B. M. Goodson, E. Y. Chekmenev, *Chem. Eur. J.*, 2015, **21**, 3156-3166.
59. S. J. Wilkens, W. M. Westler, J. L. Markley, F. Weinhold, *J. Am. Chem. Soc.*, 2001, **123**, 12026-12036
60. E. Y. Chekmenev, J. Hövener, V. A. Norton, K. Harris, L. S. Batchelder, P. Bhattacharya, B. D. Ross, D. P. Weitekamp, *J. Am. Chem. Soc.*, 2008, **130**, 4212-4213.
61. B. Heaton, *J. Am. Chem. Soc.*, 2005, **127**, 338
62. A. Shekhtman, D. S. Burz, *In-Cell NMR Spec.*, 2020
63. M. Fekete, C. Gibard, G. J. Dear, G. G. R. Green, A. J. J. Hooper, A. D. Roberts, F. Cisnetti, S. B. Duckett, *Dalton Trans.*, 2015, **44**, 7870–7880
64. P. M. Richardson, A. J. Parrott, O. Semenova, A. Nordon, S. B. Duckett, M. E. Halse, *Analyst*, 2018, **143**, 3442-3450.
65. A. Manoharan, P. J. Rayner, M. Fekete, W. Iali, P. Norcott, V. H. Perry, S. B. Duckett, *Chem. Phys. Chem.*, 2019, **20**, 285-294.
66. O. Semenova, P. M. Richardson, A. J. Parrott, A. Nordon, M. E. Halse, S. B. Duckett, *Anal. Chem.*, 2019, **91**, 6695-6701.
67. S. S. Roy, K. M. Appleby, E. J. Fear, S. B. Duckett, *J. Phys. Chem. Lett.*, 2018, **9**, 1112-1117.
68. J. Park, Y. Shin, T. H. Kim, D. H. Kim, A. Lee, (2019). *PLoS ONE*, 2019, **12**
69. J. Kurhanewicz, D. B. Vigneron, K. Brindle, E. Y. Chekmenev, A. Comment, C. H. Cunningham, R. J. Deberardinis, G. G. Green, M. O. Leach, S. S. Rajan, R. R. Rizi, B. D. Ross, W. S. Warren, C. R. Malloy, *Neoplasia*, 2011, **13**, 81-97.
70. S. Meier, P. R. Jensen, M. Karlsson, M. H. Lerche, *Sensors*, 2014, **14**, 1576-1597.
71. T. B. R. Robertson, L. H. Antonides, N. Gilbert, S. L. Benjamin, S. K. Langley, L. J. Munro, O. B. Sutcliffe, R. E. Mewis, *ChemistryOpen*, 2019, **8**, 1375-1382.
72. R. V. Shchepin, D. A. Barskiy, A. M. Coffey, T. Theis, F. Shi, W. S. Warren, B. M. Goodson, E. Y. Chekmenev, *ACS Sens*, 2016, **6**, 640-644.
73. R. Baran, *Heterocyclic Chemistry*  
<https://www.scripps.edu/baran/heterocycles/Essentials1-2009.pdf>, Accessed September 2021
74. M. Fekete, F. Ahwal, S. B. Duckett, *J. Phys. Chem.*, 2020, **124**, 4573–4580
75. A.-H. Emwas, Z. A. Al-Talla, N. Kharbatia, *Metabonomics*, 2015, **1277**, 91-112
76. T. B. R. Robertson, Development of Signal Amplification By Reversible Exchange (SABRE) towards biological and forensic applications, <https://e-space.mmu.ac.uk/626096>, Accessed September 2021
77. Y. Kawagoe, K. Moriyama, H. Togo, *Eur. J. Org. Chem.*, 2014, **19**, 4115-4122
78. F. Henry, *J. of the Am. Chem. Soc.*, 1954, **76**, 290
79. S. Pellizzari, *Gazzetta Chimica Italiana*, 1905, **35**, 375
80. P. M. Wood, L. W. Lawrence Woo, A. Humphreys, S. K. Chander, A. Purohit, M. J. Reed, B. V. L. Potter, *J. Steroid Biochem. Mol. Biol.*, 2005, **94**, 123-130
81. S. Hayat, A.-ur-Rahman, M. I. Choudhary, K. M. Khan, W. Schumann, E. Bayer, *Tetrahedron*, 2001, **57**, 9951-9957
82. G.-P. Lu, Y.-M. Lin, *J. of Chem. Research*, 2014, **38**, 371-374
83. J. Doiron, A. H. Soutan, R. Richard, Toure, M. Mamadou, N. Picot, R. Richard, M. Cuperlovic-Culf, G. A. Robichaud, M. Touaibia, *Eur. J. Med. Chem.*, 2011, **46**, 4010-4024

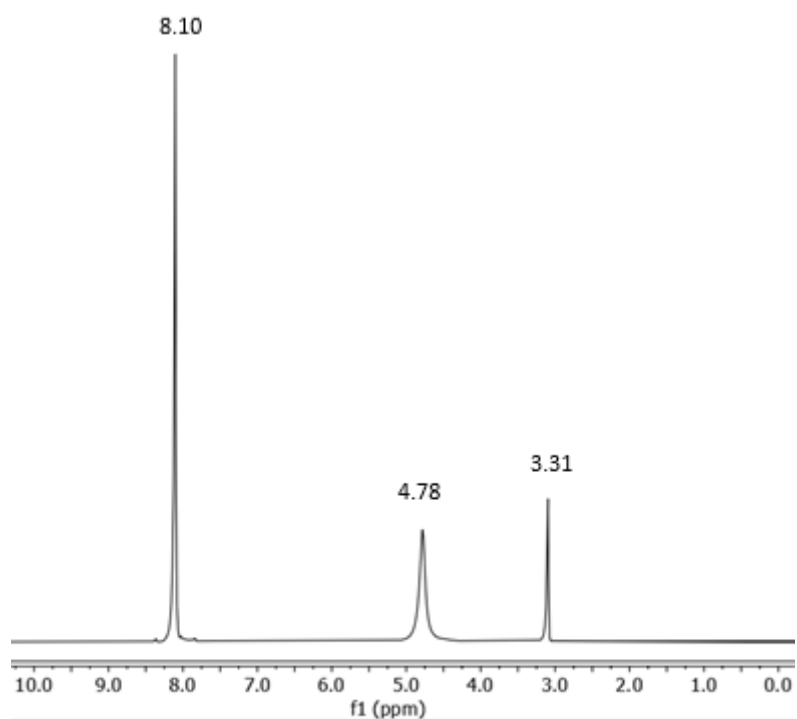
84. K. Schwärzer, C. P. Tüllmann, S. Graßl, B. Górski, C. E. Brocklehurst, P. Knochel, *Org. Lett.*, 2020, **22**, 1899-1902
85. R. Bohlmann, *Compr. Org. Synth.*, 1991, **6**, 203-223
86. Substitution reactions of alkyl halides: two mechanisms, 2020, <https://chem.libretexts.org/@go/page/14778> Accessed February 2021
87. L. Morsch, *The SN2 Mechanism*, 2019
88. F. Vatansever, M. R. Hamblin, *Photonics Lasers Med.*, 2012, **4**, 255-266.
89. A. O. Elzoghby, S. K. Mostafa, M. W. Helmy, M. A. ElDemellawy, S. A. Sheweita, *Pharm. Research*, 2017, **34**, 1956-1969
90. A. Kumar, P. Sharma, B. L. Kalal, L. K. Chandel, *J. Inclusion Phenom. Macrocyclic Chem.*, 2010, **68**, 369-379
91. M. Suman, B. Vijayabhaskar, K. NageswaraRao; S. Kumar; B. VenkateswaraRao, *Arkivoc*, 2019, **2019**, 1-8
92. M. Dračinský, P. Bouř, *J. Chem. Theory Comput.*, 2010, **6**, 288-299
93. R. M. Silverstein, G. C. Bassler, T. C. Morrill, *J. Chem. Educ.*, 1962, **5**, 546
94. X. Zhang, A. Xia, H. Chen, Y. Liu, *Org. Lett.*, 2017, **19**, 2118-2121
95. A. Dobzhenetskiy, C. A. Gater, A. T. M. Wilcock, S. Langley, R. M. Brignall, Rachel D. C. Williamson, R. Mewis, *Chem.: Bulgarian J. Science Education*, 2019, **28**, 339-350
96. P. J. Rayner, M. J. Burns, A. M. Olaru, P. Norcott, M. Fekete, G. G. R. Green, L. A. R. Highton, R. E. Mewis, S. B. Duckett, *Proc. Natl. Acad. Sci.*, 2017, **114**, 3188-3194
97. A. N. Lane, J.-F. Lefèvre, O. Jardetzky, *J. Magn. Reson.*, 1986, **66**, 201-218.
98. C. S. Weinert, *ISRN Spectroscopy*, 2012, **2012**, 1-18
99. H. Zeng, J. Xu, J. Gillen, M. T. McMahon, D. Artemov, J.-M. Tyburn, J. A. B. Lohman, R. E. Mewis, K. D. Atkinson, G. G. R. Green, S. B. Duckett, P. C. M. van Zijl, *J. Magn. Reson.*, 2013, **237**, 73-78
100. I. J. Day, J. C. Mitchell, M. J. Snowden, A. L. Davis, *Magn. Reason. Chem.*, 2007, **45**, 1018 - 1021.
101. N. K. J. Hermkens, M. C. Feiters, F. P. J. T. Rutjes, S. S. Wijmenga, M. Tessari, *J. Magn. Reson.*, 2017, **276**, 122-127
102. R. E. Mewis, R. A. Green, M. C. Cockett, M. J. Cowley, S. B. Duckett, G. G. Green, R. O. John, P. J. Rayner, D. C. Williamson, *The J. Phys. Chem.* 2015, **4**, 1416–1424

## Appendix:

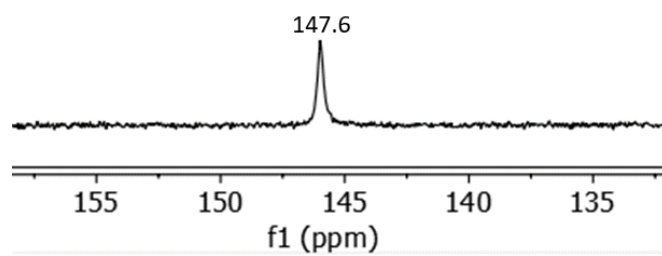
### 1,2,4-Triazole (10a)



### A1 - IR spectrum of 10a

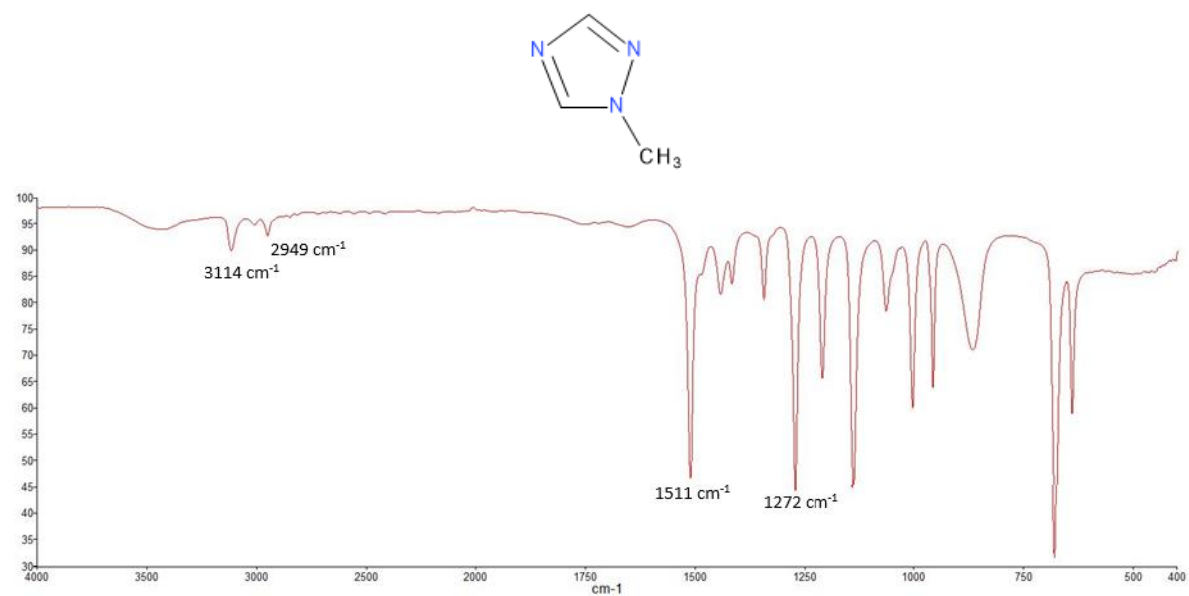


**A2** - <sup>1</sup>H NMR spectrum **10a** collected in methanol-d<sub>4</sub> (solvent peaks present at the chemical shifts δ 4.78ppm and 3.31ppm)

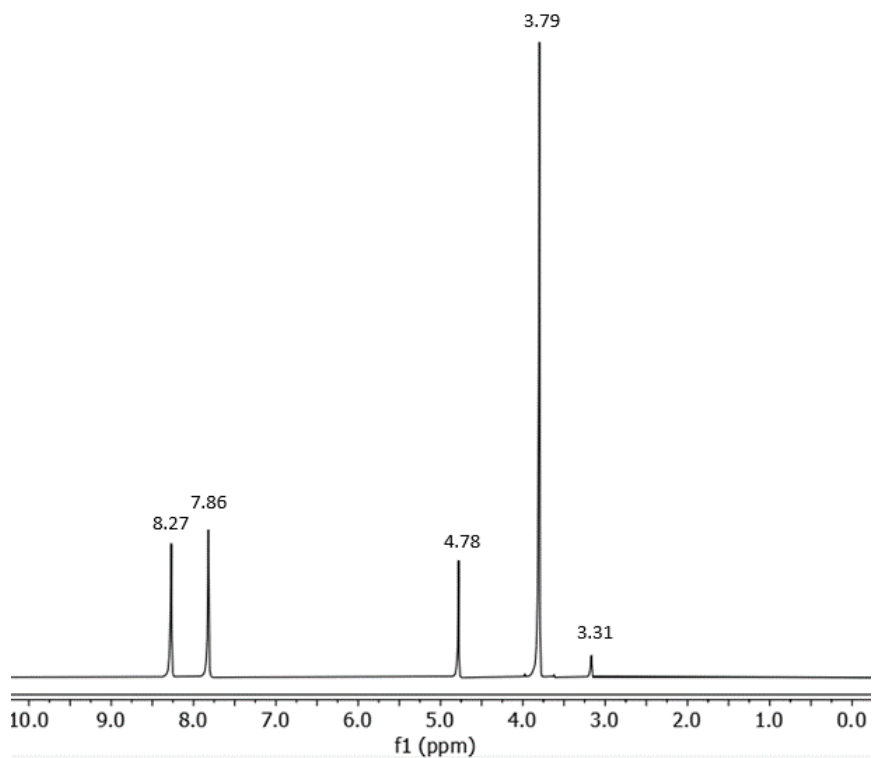


**A2a** - <sup>13</sup>C NMR spectrum **10a** collected in methanol-d<sub>4</sub> (solvent peak present at the chemical shift  $\delta$  49.15 ppm)

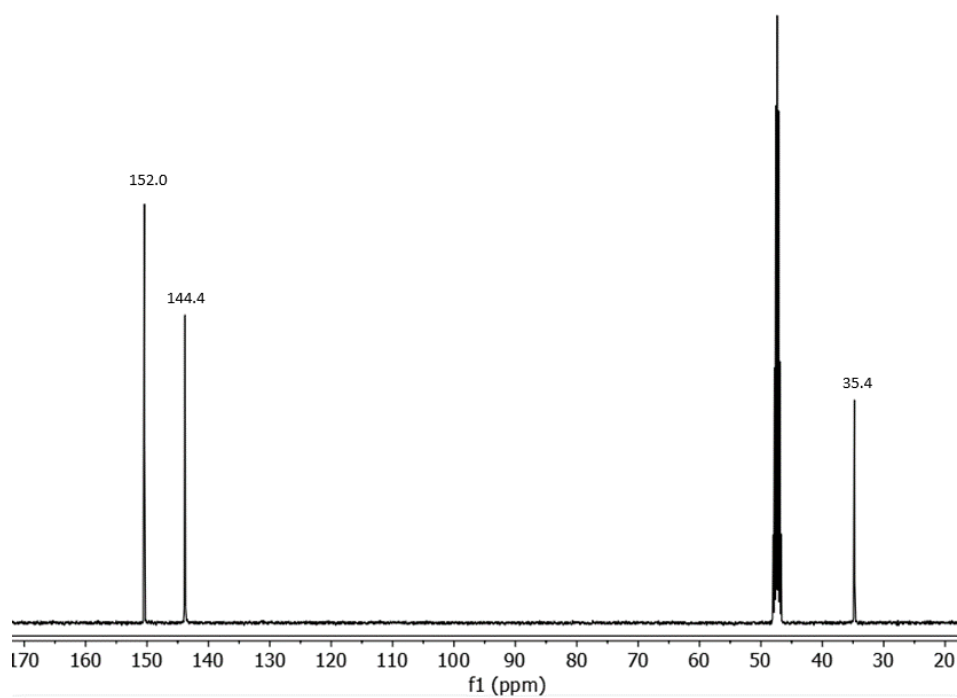
**1-methyl-1H-1,2,4-triazole (10b)**



**A3** IR spectrum of **10b**

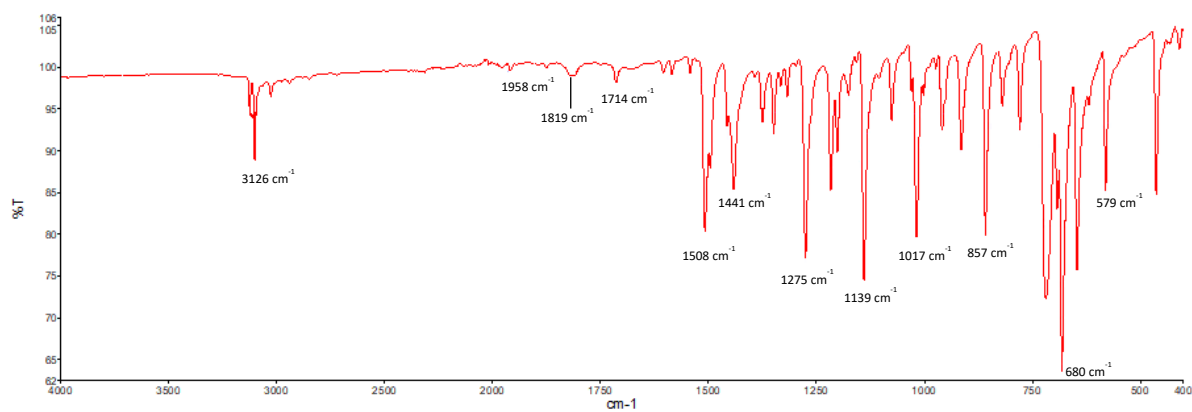
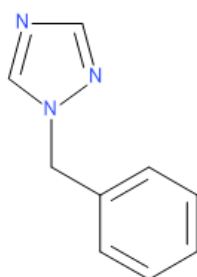


**A4** -  $^1\text{H}$  NMR spectrum **10b** collected in methanol- $\text{d}_4$  (solvent peaks present at the chemical shifts  $\delta$  4.78ppm and 3.31ppm)

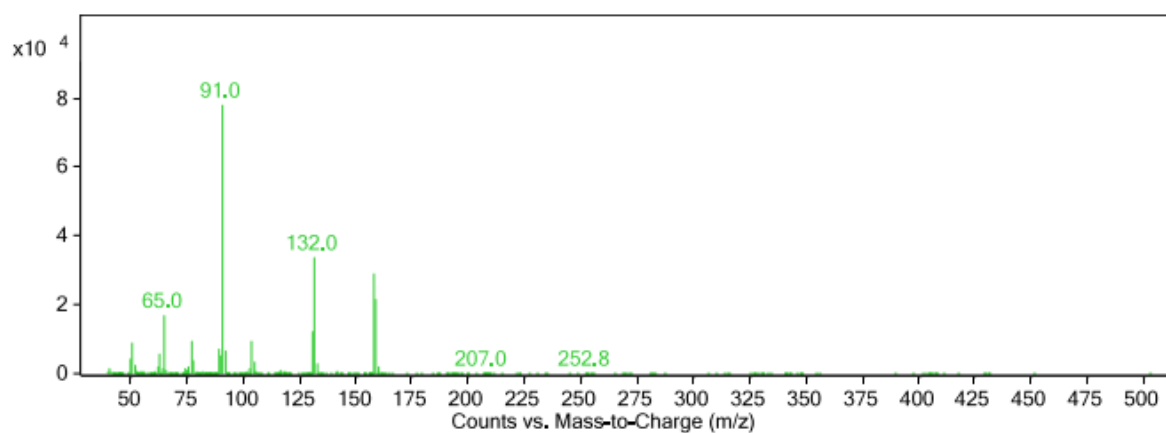


**A4a**-  $^{13}\text{C}$  NMR spectrum **10b** collected in methanol- $\text{d}_4$  (solvent peak present at the chemical shift  $\delta$  49.15 ppm)

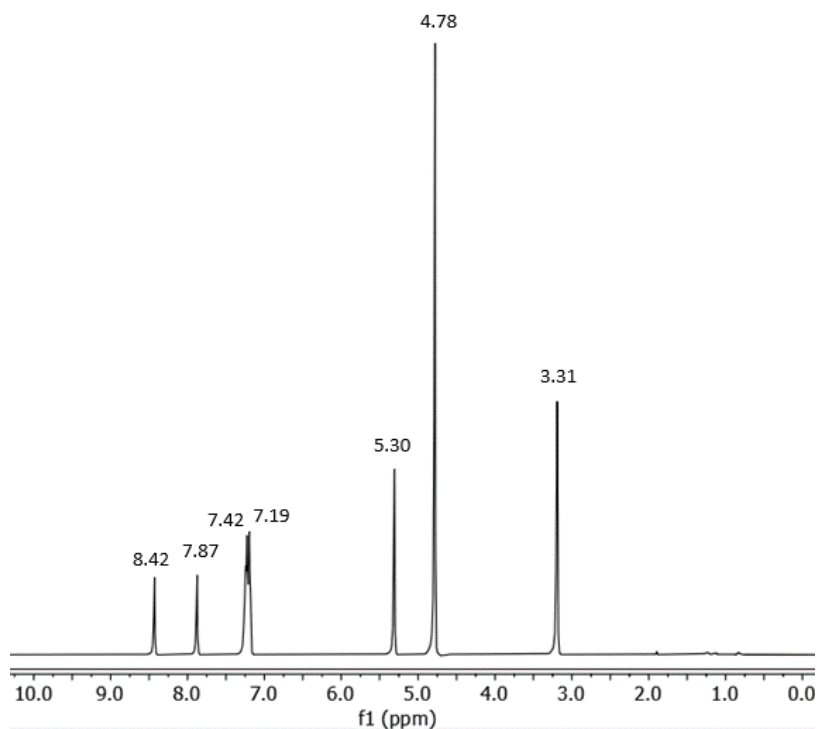
## 1-benzyl-1,2,4-triazole (10c)



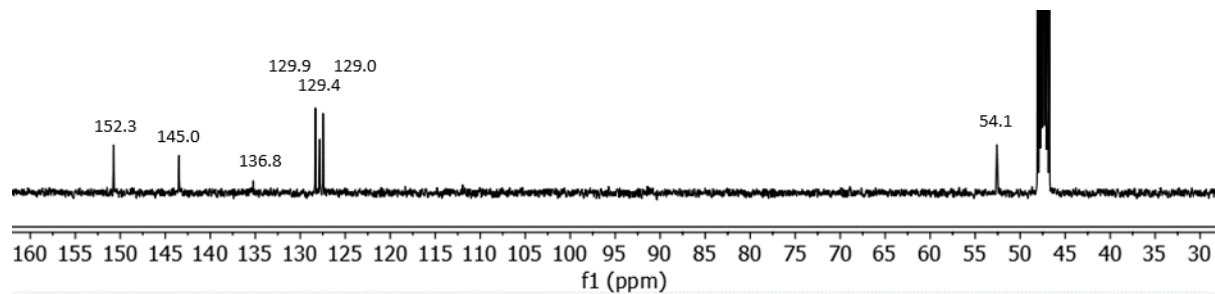
## A5 - IR spectrum of 10c



## A6 - GC-MS spectrum of 10c with visible molecular ion and base peaks as well as the corresponding structures of fragments

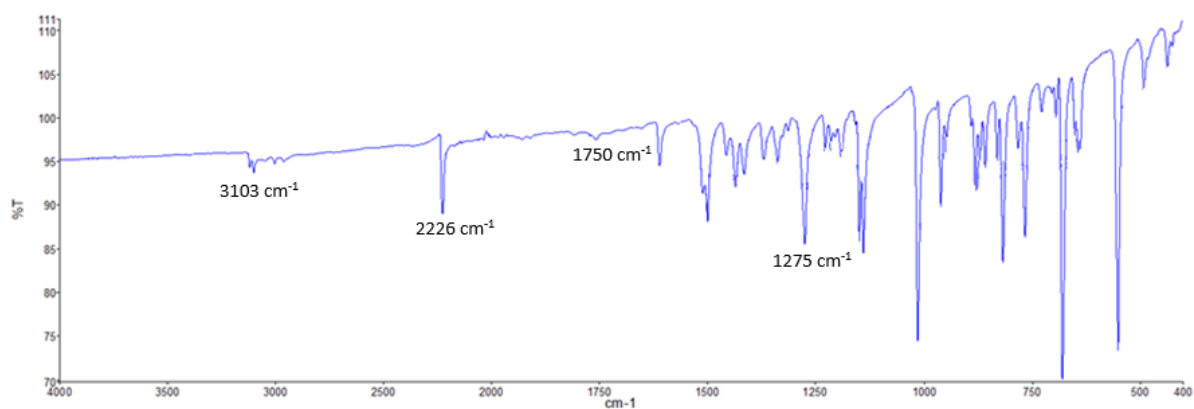
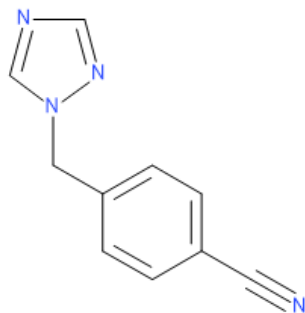


**A7** - <sup>1</sup>H NMR spectrum **10c** collected in methanol-d<sub>4</sub> (solvent peaks present at the chemical shifts δ 4.78ppm and 3.31ppm)

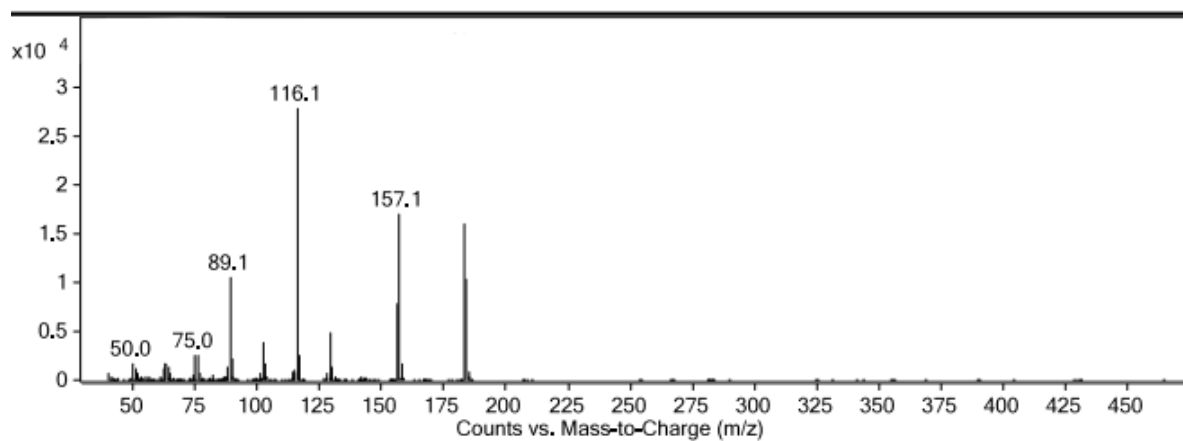


**A7a** - <sup>13</sup>C NMR spectrum **10a** collected in methanol-d<sub>4</sub> (solvent peak present at the chemical shift δ 49.15 ppm)

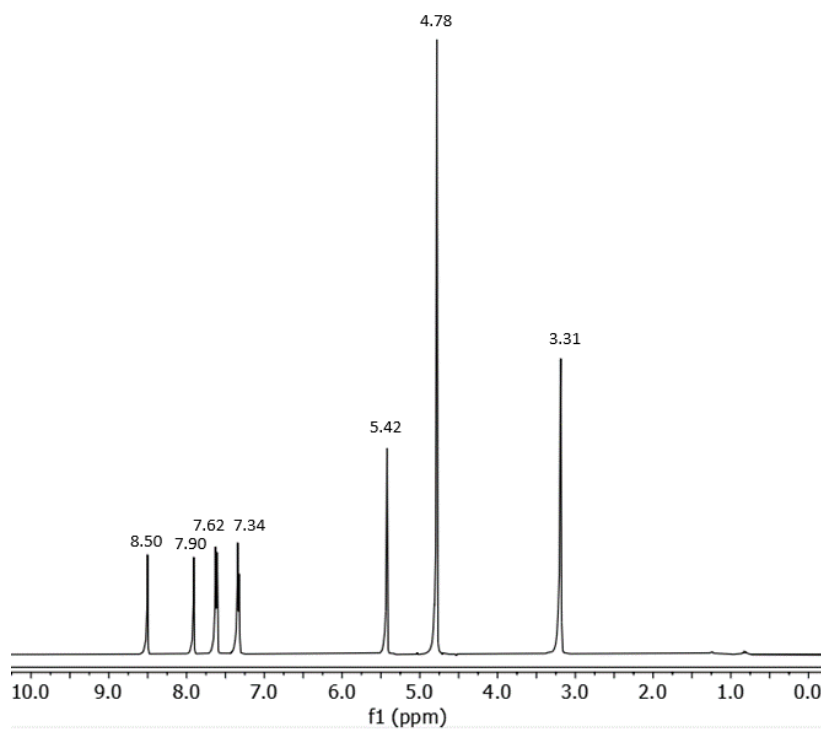
#### 4-(1H-1,2,4-Triazol-1-ylmethyl)benzonitrile (10d)



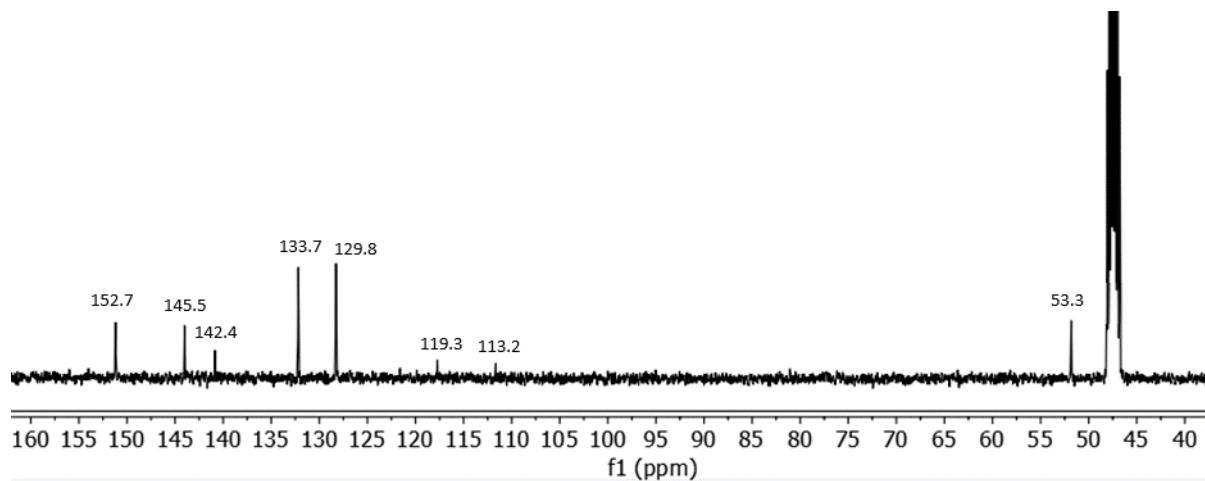
**A8** - IR spectrum of **10d**



**A9** - GC-MS spectrum of **10d** with visible molecular ion and base peaks as well as the corresponding structures of fragments

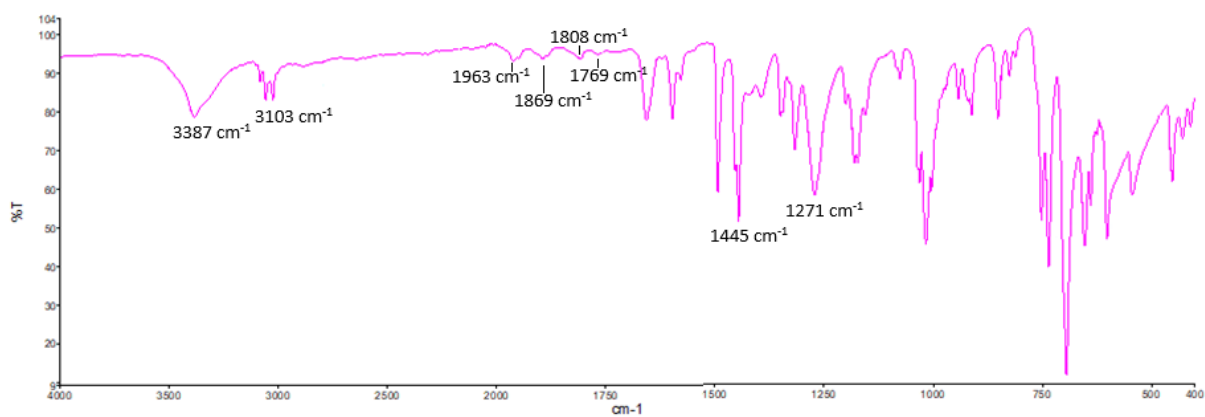
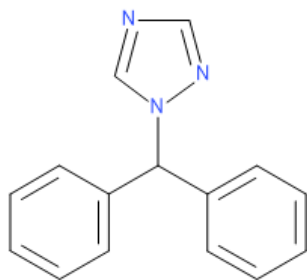


**A10** -  $^1\text{H}$  NMR spectrum **10d** collected in methanol- $\text{d}_4$  (solvent peaks present at the chemical shifts  $\delta$  4.78ppm and 3.31ppm)

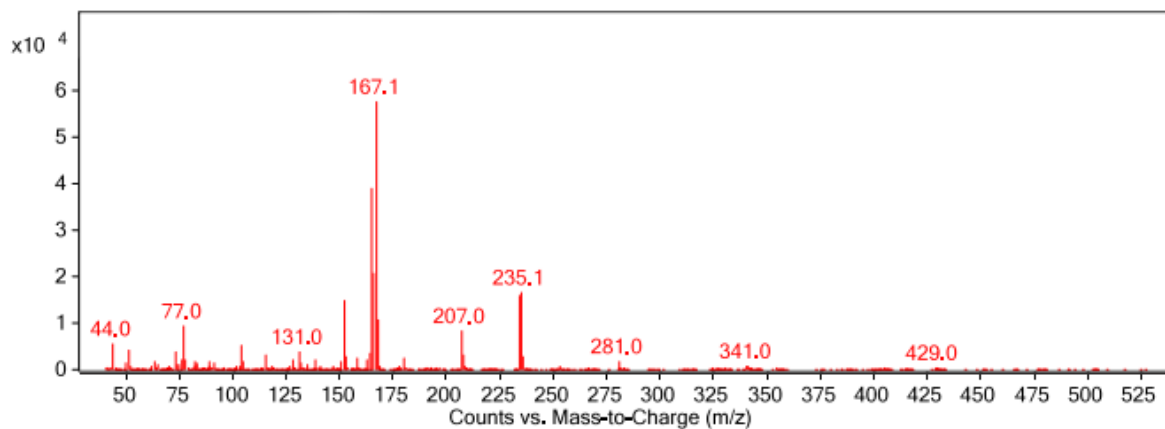


**A10a** -  $^{13}\text{C}$  NMR spectrum **10a** collected in methanol- $\text{d}_4$  (solvent peak present at the chemical shift  $\delta$  49.15 ppm)

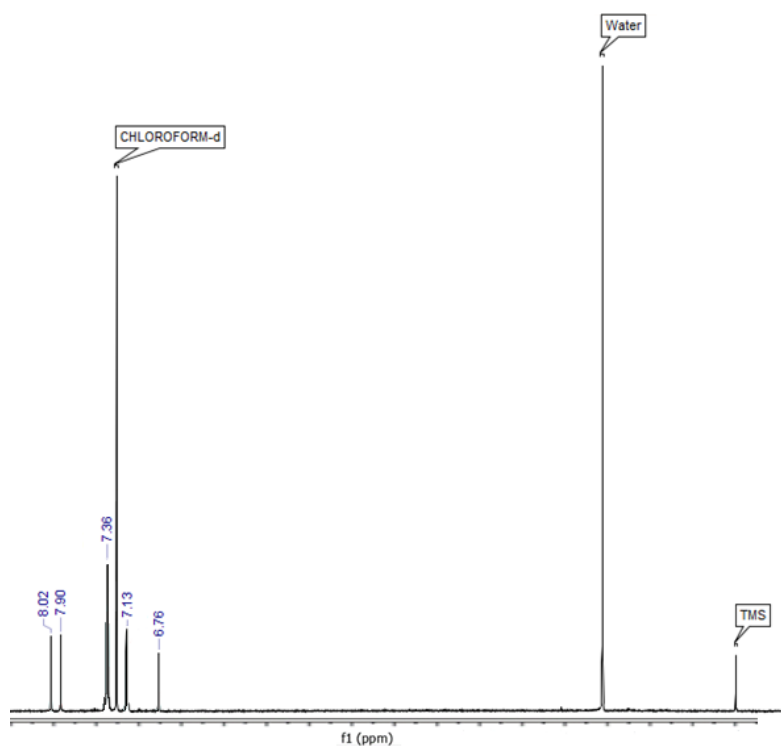
### 1-[di(phenyl)methyl]-1H-1,2,4-triazole (10e)



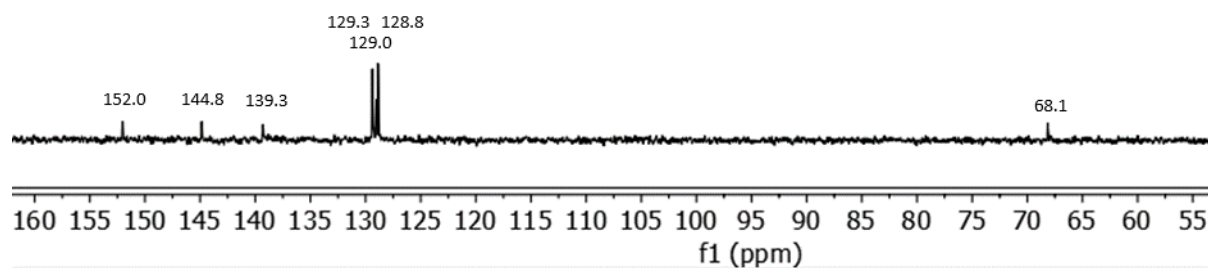
### A11 IR spectrum of 10e



**A12-** GC-MS spectrum of **10e** with visible molecular ion and base peaks as well as the corresponding structures of fragments

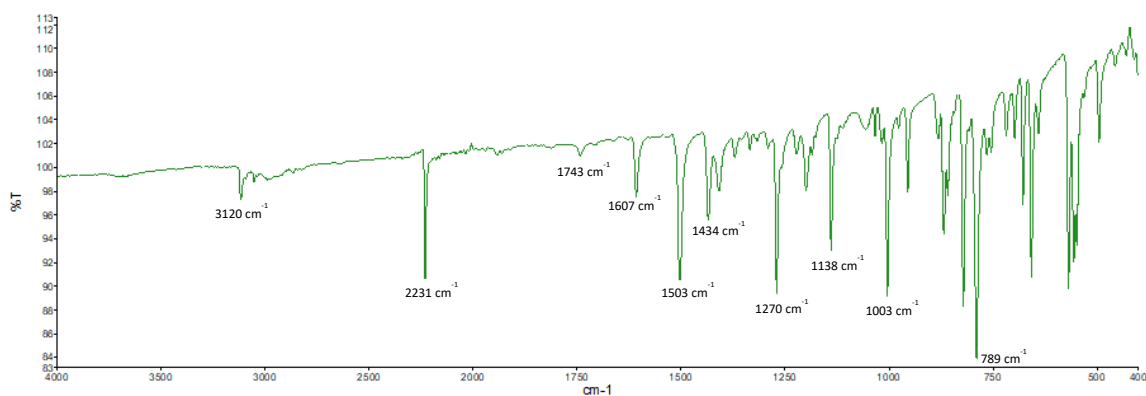
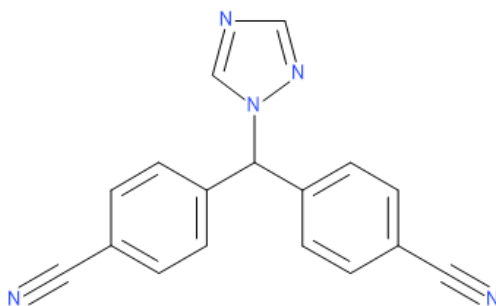


**A13-**  $^1\text{H}$  NMR spectrum **10b** collected in chloroform- $\text{d}_4$  (solvent peaks present at the chemical shifts  $\delta$  7.26ppm and water peak at the chemical shifts  $\delta$  1.6ppm)

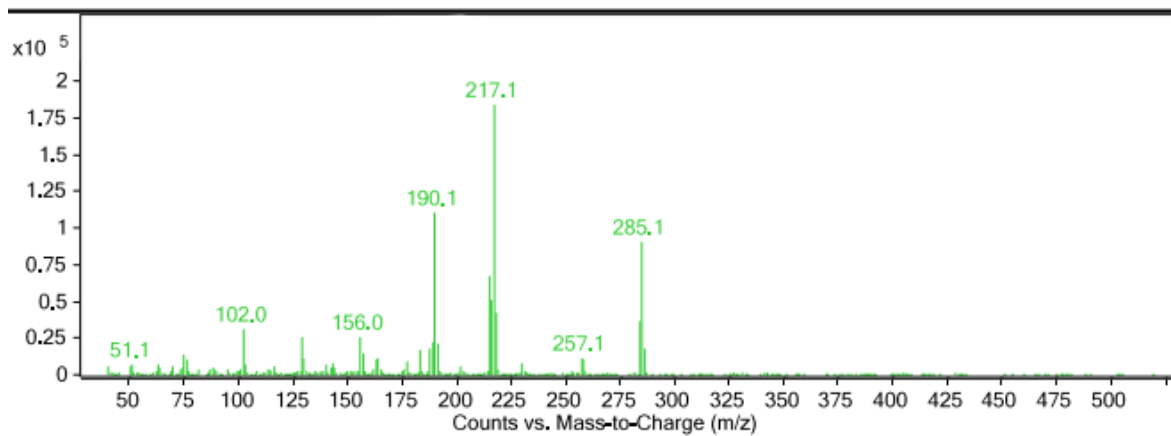


**A13a** -  $^{13}\text{C}$  NMR spectrum **10a** collected in methanol- $\text{d}_4$  (solvent peak present at the chemical shift  $\delta$  49.15 ppm)

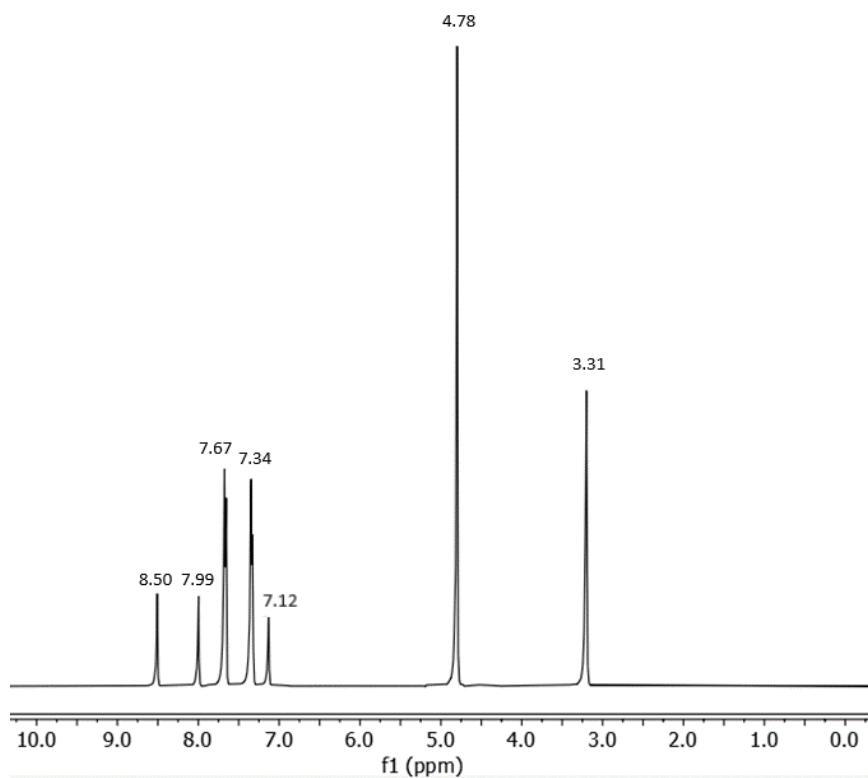
### 4-[(4-cyanophenyl)-(1,2,4-triazol-1-yl)methyl]benzonitrile (Letrozole, **3**)



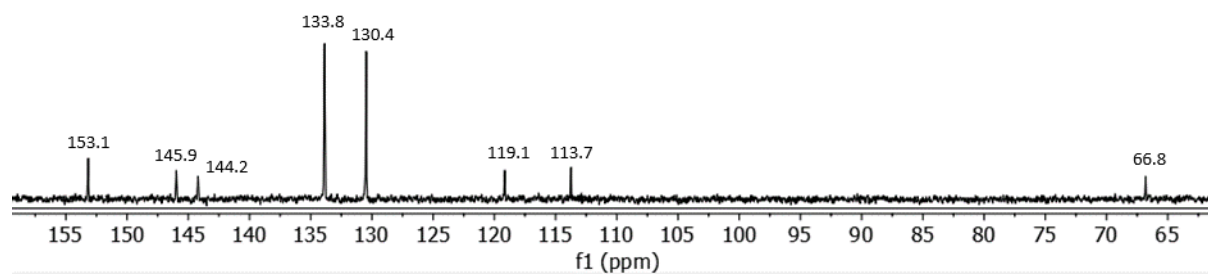
**A14** - IR spectrum of **3**



**A15** - GC-MS spectrum of **3** with visible molecular ion and base peaks as well as the corresponding structures of fragments



**A16** -  $^1\text{H}$  NMR spectrum **3** collected in methanol- $\text{d}_4$  (solvent peaks present at the chemical shifts  $\delta$  4.78ppm and 3.31ppm)



**A16a** -  $^{13}\text{C}$  NMR spectrum **3** collected in methanol- $\text{d}_4$  (solvent peak present at the chemical shift  $\delta$  49.15 ppm)